RESEARCH ARTICLE SUMMARY

DRUG DEVELOPMENT

The target landscape of clinical kinase drugs

Susan Klaeger,* Stephanie Heinzlmeir,* Mathias Wilhelm,* Harald Polzer, Binje Vick, Paul-Albert Koenig, Maria Reinecke, Benjamin Ruprecht, Svenja Petzoldt, Chen Meng, Jana Zecha, Katrin Reiter, Huichao Qiao, Dominic Helm, Heiner Koch, Melanie Schoof, Giulia Canevari, Elena Casale, Stefania Re Depaolini, Annette Feuchtinger, Zhixiang Wu, Tobias Schmidt, Lars Rueckert, Wilhelm Becker, Jan Huenges, Anne-Kathrin Garz, Bjoern-Oliver Gohlke, Daniel Paul Zolg, Gian Kayser, Tonu Vooder, Robert Preissner, Hannes Hahne, Neeme Tõnisson, Karl Kramer, Katharina Götze, Florian Bassermann, Judith Schlegl, Hans-Christian Ehrlich, Stephan Aiche, Axel Walch, Philipp A. Greif, Sabine Schneider, Eduard Rudolf Felder, Juergen Ruland, Guillaume Médard, Irmela Jeremias, Karsten Spiekermann, Bernhard Kuster†

INTRODUCTION: Molecularly targeted drugs such as imatinib and crizotinib have revolutionized the treatment of certain blood and lung cancers because of their remarkable clinical success. Over the past 20 years, protein kinases have become a major class of drug targets because these signaling biomolecules are often deregulated in disease, particularly in cancer. Today, 37 small kinase inhibitors (KIs) are approved medicines worldwide and more than 250 drug candidates are undergoing clinical evaluation.

RATIONALE: Although it is commonly accepted that most KIs target more than one protein, the extent to which this information is available to the public varies greatly between drugs. It would seem important to thoroughly characterize the target spectrum of any drug because additional off-targets may offer opportunities, not only for repurposing but also to explain undesired side effects. To this end, we used a chemical proteomic approach (kinobeads) and quantitative mass spectrometry to characterize the target space of 243 clinical KIs that are approved drugs or have been tested in humans.

RESULTS: The number of targets for a given drug differed substantially. Whereas some compounds showed exquisite selectivity, others targeted more than 100 kinases simultaneously, making it difficult to attribute their biological effects to any particular mode of action. Also of note is that recently developed irreversible KIs can address more kinases than their intended targets epidermal growth factor receptor (EGFR) and Bruton's tyrosine kinase (BTK). Collectively, the evaluated KIs targeted 220 kinases with submicromolar affinity, offering a view of the druggable kinome and enabling the development of a universal new selectivity metric termed CATDS (concentration- and target-dependent selectivity). All drug profiles can be interactively explored in ProteomicsDB and a purpose-built shinyApp. Many uses of this unique data and analysis resource by the scientific community can be envisaged, of which we can only highlight a few. The profiles identified many new targets for established drugs, thus improving our understanding of how these drugs might exert their phenotypic effects. For example, we evaluated novel salt-inducible kinase 2 (SIK2) inhibitors for their ability to modulate tumor necrosis factor–α (TNFα) and interleukin-10 (IL-10) production, which may allow repurposing these drugs for inflammatory conditions. Integrating target space information with phosphoproteomic analysis of several EGFR inhibitors enabled the identification of drug response markers inside and outside the canonical EGFR signaling pathway. Off-target identification may also inform drug discovery projects using high-value clinical molecules as lead compounds. We illustrate such a case by a novel structure-affinity relationship analysis of MELK inhibitors based on target profiles and cocrystal structures. To assess the repurposing potential of approved or clinically advanced compounds, we used cell-based assays and mouse xenografts to show that golvatinib and cabozantinib may be used for the treatment of acute myeloid leukemia (AML) based on their FLT3 inhibitory activity.

CONCLUSION: This work provides a rich data resource describing the target landscape of 243 clinically tested KIs. It is the most comprehensive study to date and illustrates how the information may be used in basic research, drug discovery, or clinical decision-making. ■

ON OUR WEBSITE

Read the full article at http://dx.doi.org/10.1126/science.aan4368

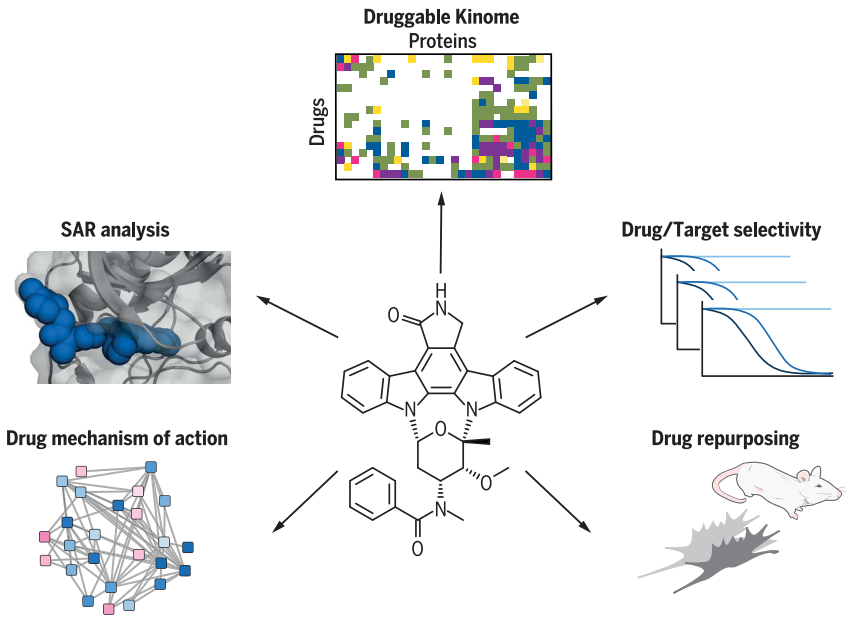

Schematic representation of identifying the druggable kinome. A chemical proteomic approach revealed quantitative interaction profiles of 243 clinically evaluated small-molecule KIs covering half of the human kinome. Results can be interactively explored in ProteomicsDB and inform basic biology, drug discovery, and clinical decision-making.

The list of author affiliations is available in the full article online.
*These authors contributed equally to this work.
†Corresponding author. Email: kuster@tum.de
Cite this article as S. Klaeger *et al.*, *Science* **358**, eaan4368 (2017). DOI: 10.1126/science.aan4368

Downloaded from http://science.sciencemag.org/ on November 30, 2017

RESEARCH ARTICLE

DRUG DEVELOPMENT

The target landscape of clinical kinase drugs

Susan Klaeger,[1,2,3]* Stephanie Heinzlmeir,[1,2,3]* Mathias Wilhelm,[1]* Harald Polzer,[2,3,4] Binje Vick,[2,3,5] Paul-Albert Koenig,[6] Maria Reinecke,[1,2,3] Benjamin Ruprecht,[1] Svenja Petzoldt,[1,2,3] Chen Meng,[1] Jana Zecha,[1,2,3] Katrin Reiter,[2,3,4] Huichao Qiao,[1] Dominic Helm,[1] Heiner Koch,[1,2,3] Melanie Schoof,[1] Giulia Canevari,[7] Elena Casale,[7] Stefania Re Depaolini,[7] Annette Feuchtinger,[8] Zhixiang Wu,[1] Tobias Schmidt,[1] Lars Rueckert,[9] Wilhelm Becker,[9] Jan Huenges,[9] Anne-Kathrin Garz,[2,3,10] Bjoern-Oliver Gohlke,[2,3,11] Daniel Paul Zolg,[1] Gian Kayser,[12] Tonu Vooder,[13,14,15] Robert Preissner,[2,3,11] Hannes Hahne,[1] Neeme Tõnisson,[14,15] Karl Kramer,[1] Katharina Götze,[2,3,10] Florian Bassermann,[2,3,10] Judith Schlegl,[16] Hans-Christian Ehrlich,[9] Stephan Aiche,[9] Axel Walch,[8] Philipp A. Greif,[2,3,4] Sabine Schneider,[17,18] Eduard Rudolf Felder,[7] Juergen Ruland,[2,3,6] Guillaume Médard,[1] Irmela Jeremias,[2,5,19] Karsten Spiekermann,[2,3,4] Bernhard Kuster[1,2,3,18,20]†

Kinase inhibitors are important cancer therapeutics. Polypharmacology is commonly observed, requiring thorough target deconvolution to understand drug mechanism of action. Using chemical proteomics, we analyzed the target spectrum of 243 clinically evaluated kinase drugs. The data revealed previously unknown targets for established drugs, offered a perspective on the "druggable" kinome, highlighted (non)kinase off-targets, and suggested potential therapeutic applications. Integration of phosphoproteomic data refined drug-affected pathways, identified response markers, and strengthened rationale for combination treatments. We exemplify translational value by discovering SIK2 (salt-inducible kinase 2) inhibitors that modulate cytokine production in primary cells, by identifying drugs against the lung cancer survival marker MELK (maternal embryonic leucine zipper kinase), and by repurposing cabozantinib to treat FLT3-ITD–positive acute myeloid leukemia. This resource, available via the ProteomicsDB database, should facilitate basic, clinical, and drug discovery research and aid clinical decision-making.

Many of the 518 protein kinases encoded by the human genome have emerged as drug targets because their function is often deregulated in signal transduction networks, leading to diseases such as cancer and inflammation. More than 250 kinase inhibitors (KIs) are currently undergoing clinical trials, and 37 have been approved for human use (*1*). Half of the approvals occurred within the past 4 years, demonstrating the continued importance of protein kinases as a target class (*2*). Owing to the fact that many compounds target the structurally and functionally conserved adenosine 5′-triphosphate (ATP)–binding site, polypharmacology (that is, drugs that act on more than one target) is commonly observed. Target promiscuity may have advantageous or detrimental therapeutic consequences. Thus, it is important to thoroughly investigate the target space of these molecules to understand the molecular and cellular mechanisms of action (MoAs). To this end, several kinase activity and binding screens have been published (*3*–*12*). Despite the considerable value of these studies, the target space of most clinically evaluated KIs has not yet been systematically analyzed. In addition, recombinant kinase assays cannot capture many of the regulating factors provided by a full-length protein expressed in a native cellular context (for example, posttranslational modifications, protein complex interactions, or the presence of metabolites). Here, the target space, selectivity, and full dose-response characteristics of 243 clinical (that is, tested in humans) KIs were investigated by chemical proteomics using lysates of cancer cells, kinobeads, and quantitative mass spectrometry (MS) (*13*, *14*). This is currently the largest publicly available information resource for clinical drug-target interactions. We highlight utility in identifying novel targets for established drugs and for the repurposing of existing drugs for new targets or disease indications. All data can be interactively explored in the ProteomicsDB database (*15*) to facilitate translational research and kinase drug discovery in academia, biotech, and pharma as well as clinical decision-making.

Chemoproteomic target screen of 243 clinical KIs

To determine the protein targets of the 243 KIs, a quantitative, MS-based chemical proteomic assay termed kinobeads was used (*13*, *14*). Briefly, kinobeads feature immobilized broad-spectrum KIs that enable the purification of endogenous kinases from cells or tissues. When performed as a competition binding assay and measured by quantitative MS, kinobeads allow the label-free measurement of the physical interaction of a compound of interest with thousands of proteins in parallel. Here, KIs were dosed at eight concentrations (plus vehicle and target depletion control) to derive dose-response characteristics and apparent dissociation constants (K_d^{app}) for every drug-protein interaction (Fig. 1A, fig. S1A, tables S1 to S3, and supplementary text). Quantification of protein binding by MS essentially yielded the same data as Western blot analysis (fig. S1B) but does not require antibodies and affords much higher throughput for target proteins. Kinobeads assay data also agreed well with the KiNativ technology (*16*), which is an alternative binding assay using covalent ATP probes (fig. S1C). The correlation of kinobeads binding and enzymatic activity data was good but not quite as strong as between the two binding methods (fig. S1D), and reasons for the observed discrepancies have been discussed before (*16*–*18*). For example, the activation status of an endogenous kinase in cells may not be the same as that of a recombinant protein in a cell-free system. In addition, the high protein concentration of lysates can lead to various degrees of unspecific binding of the generally hydrophobic KIs akin to the extensive binding of most drugs to plasma proteins. Despite the above, we observed that when a compound scored in the kinobeads assay, it also inhibited the activity of

[1]Chair of Proteomics and Bioanalytics, Technical University of Munich (TUM), Freising, Germany. [2]German Cancer Consortium (DKTK), Heidelberg, Germany. [3]German Cancer Research Center (DKFZ), Heidelberg, Germany. [4]Department of Internal Medicine III, University Hospital, Ludwig-Maximilians-Universität (LMU) München, Munich, Germany. [5]Department of Apoptosis in Hematopoietic Stem Cells, Helmholtz Center Munich, German Center for Environmental Health (HMGU), Munich, Germany. [6]Institut für Klinische Chemie und Pathobiochemie, TUM, Munich, Germany. [7]Oncology, Nerviano Medical Sciences Srl, Milan, Italy. [8]Research Unit Analytical Pathology, Helmholtz Zentrum München, Neuherberg, Germany. [9]SAP SE, Potsdam, Germany. [10]Department of Medicine III, Klinikum rechts der Isar, TUM, Munich, Germany. [11]Structural Bioinformatics Group, Charité-Universitätsmedizin, Berlin, Germany. [12]Institute of Surgical Pathology, University Medical Center Freiburg, Faculty of Medicine, University of Freiburg, Freiburg, Germany. [13]Center of Thoracic Surgery, Krefeld, Germany. [14]Estonian Genome Center, University of Tartu, Tartu, Estonia. [15]Tartu University Hospital, Tartu, Estonia. [16]SAP SE, Walldorf, Germany. [17]Department of Chemistry, TUM, Garching, Germany. [18]Center For Integrated Protein Science Munich (CIPSM), Munich, Germany. [19]Department of Pediatrics, Dr von Hauner Children's Hospital, LMU, Munich, Germany. [20]Bavarian Biomolecular Mass Spectrometry Center (BayBioMS), TUM, Freising, Germany.
*These authors contributed equally to this work.
†Corresponding author. Email: kuster@tum.de

Downloaded from http://science.sciencemag.org/ on November 30, 2017

the kinase in a recombinant kinase assay (but not vice versa), showing that the kinobeads interaction data obtained in complex cell lysates can be functionally interpreted.

To define the target space that can be addressed by the kinobeads assay, RNA sequencing, full proteome profiling, and kinobeads measurements were performed for the four cell lines used in the interaction screen [K-562, MV-4-11, SK-N-BE(2), and COLO 205], and a total of 494 transcribed kinases (including mutations), 363 translated kinases, and 253 kinases on kinobeads were identified (fig. S1, E and F, and tables S4 and S5). Some kinases (for example, MET) were too weakly expressed in the cell lines used to be robustly detected but were observed when using an alternative cell line (12 MET inhibitors were also profiled in CAKI cells; fig. S1G). Some kinases escaped detection entirely as the immobilized probes were unable to capture them. A few kinases were not competed even by excess compound because the proteins bound to beads by an unknown binding mode. This was pronounced for members of the phosphatidylinositol 3-kinase (PI3K)/mammalian target of rapamycin (mTOR) family, and when an immobilized derivative of the PI3K/mTOR inhibitor omipalisib was used, these proteins also became amenable to the assay (fig. S1H). Some KIs are known to bind G protein (guanine nucleotide–binding protein)–coupled receptors (GPCRs) (*10*), but these cannot be assayed by kinobeads because we have not detected binding of any GPCRs to the five immobilized KIs that constitute kinobeads.

Unsupervised clustering of pK_d^{app} (negative logarithm of apparent dissociation constants K_d^{app} in molar) values for all inhibitors and the targeted kinases obtained from ~3000 affinity purifications (Fig. 1B) offered a view of the kinome that can be drugged by current clinical KIs. The systematic collection of these quantitative drug-target interaction profiles revealed groups of drugs for intended or phylogenetically related targets [for example, cyclin-dependent kinases (CDKs) and protein kinase C (PKC)]. Historically, drug discovery focused on tyrosine kinases and, not surprisingly, these form a large cluster, as do multikinase inhibitors with very promiscuous target profiles.

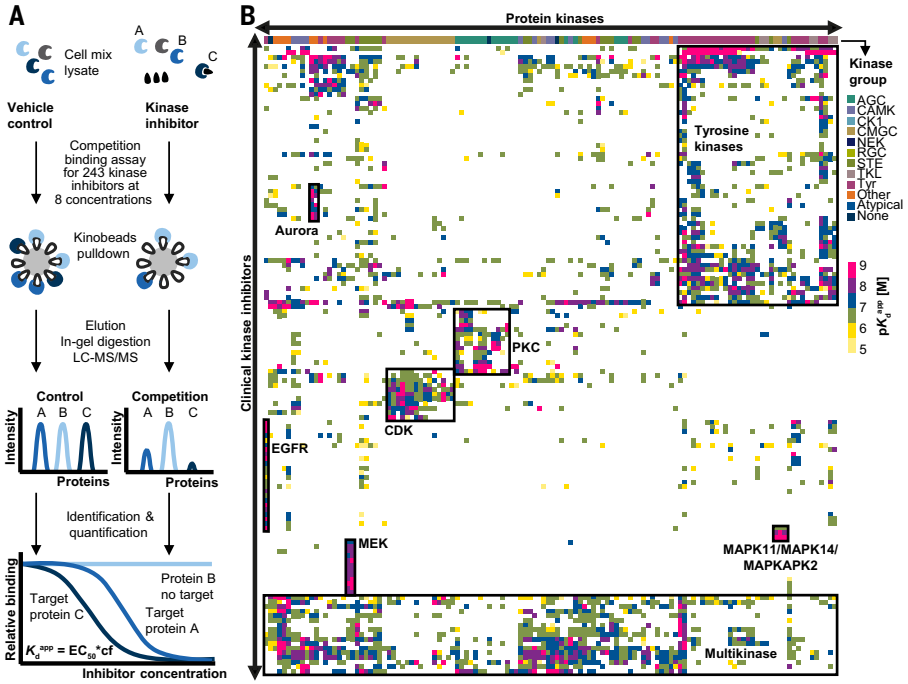

Fig. 1. The "druggable" kinome. (**A**) Schematic representation of the chemical proteomic workflow used to profile drug-protein interactions. Cell lysates were separately equilibrated with vehicle or increasing concentrations of each drug. Kinobeads were used to enrich kinases and other proteins from each lysate. Proteins were eluted from the beads, digested with trypsin, identified by liquid chromatography–tandem MS (LC-MS/MS), and quantified using the MS intensity of the identified peptides. Nonlinear regression determined the effective drug concentration, at which half of the target protein was competed [median effective concentration (EC_{50})]. EC_{50} values were converted into apparent dissociation constants (K_d^{app}) of each drug-target interaction by correcting for the depletion of a target protein from the lysate by kinobeads [correction factor (cf)]. This workflow enabled the simultaneous measurement of interaction of one drug with hundreds of proteins in a single experiment. (**B**) Hierarchical clustering of kinase targets against clinical kinase drugs provided an overview of the druggable kinome (color code depicts the K_d^{app} of drug-target interactions). Boxed regions represent groups of kinases and inhibitors that ranged from highly selective (for example, EGFR or MEK inhibitors) to relatively unselective interactions (for example, tyrosine kinase and multikinase inhibitors). Further details are provided in figs. S1 and S2 and tables S2 and S3.

In contrast, the map also indicates that some inhibitors are quite selective, for example, drugs targeting MAP2K1 [mitogen-activated protein kinase (MAPK) kinase (MEK)], MAPK11/14 (p38), or epidermal growth factor receptor (EGFR). To the best of our knowledge, the present work constitutes the most comprehensive drug-target interaction analysis for KIs to date. Broad binding or activity profiles for KIs may exist within drug discovery programs in the pharmaceutical or biotech industry but are generally not available to academic laboratories working with these molecules. Therefore, every drug-target profile provides valuable information as to how these compounds may exert their effects, how they may be used in the laboratory, and if any particular effect can be attributed to the targeting of a particular protein. To facilitate the use of the present work, all drug-target profiles generated in this study are provided as PDF files (see fig. S2 for an example) on ProteomeXchange (www.proteomexchange.org/) and can be interactively explored in ProteomicsDB (www.proteomicsdb.org) as well as in a purpose-built selectivity calculator (http://129.187.44.58:7575/).

Selective chemical probes and polypharmacology

Many clinical KIs are claimed to be potent and selective; however, this is often not the case, resulting in failure of clinical trials and obstacles with laboratory research. Assessing selectivity of a compound for a target or target class is not a trivial undertaking, because the full range of targets (and their cellular expression levels or concentrations) is often unknown and the complete compound dose range is rarely measured. All KIs in our study were profiled in a dose-dependent manner and at near thermodynamic equilibrium in cellular lysates. Thus, this large body of binding data enabled the development of a new selectivity metric termed CATDS (concentration- and target-dependent selectivity) that goes beyond previously published selectivity scores (*3*, *5*, *19*–*21*) in that it also captures aspects of target engagement and drug MoA. CATDS measures the reduction of binding of a particular protein to kinobeads at a particular compound concentration relative to the summed reduction of binding of all proteins at that concentration. Therefore, a CATDS value close to one or close to zero is indicative of selective and unselective compounds, respectively (fig. S3 and table S6; see supplementary text for a more detailed discussion).

CATDS analysis of drugs in this study not only confirmed many previous observations but also revealed some surprises. Some molecules appeared to be very selective (for example, capmatinib for MET, lapatinib for EGFR, and rabusertib for CHEK1; in general scores > 0.5; Fig. 2A) and may thus qualify as chemical probes for these targets. Compounds in blue were previously classified as selective probes in www.chemicalprobes.org/ (*22*), but many of these showed rather poor selectivity in our assay. Perhaps more surprisingly, clinically more advanced compounds did not show higher selectivity than those from earlier trial phases. This reinforces the notion that selectivity is not

Downloaded from http://science.sciencemag.org/ on November 30, 2017

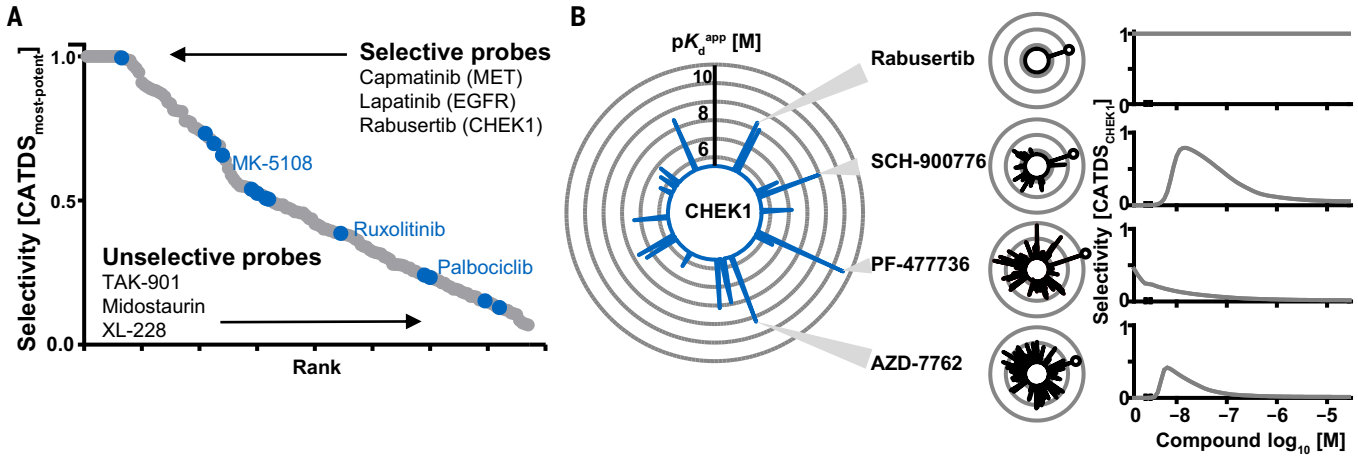

Fig. 2. Selectivity of KIs. The collective drug-protein interaction data enabled the definition of a new selectivity metric (CATDS). CATDS measures the reduction in binding of a target protein to kinobeads at a specified concentration relative to the summed reduction of all protein targets of the compound at the same concentration. (**A**) Rank plot of KIs according to CATDS$_{most\text{-}potent}$ (most potent compound target at the respective K_d^{app}) showing that lapatinib, capmatinib, and rabusertib are highly selective inhibitors, whereas TAK-901, midostaurin, and XL-228 are not. Compounds previously designated as "chemical probes" are shown in blue but are not necessarily selective. (**B**) The large radar plot shows all CHEK1 inhibitors (each spoke is a drug, and the length of the spoke is indicative of binding affinity). The smaller plots depict the number and potency of targets for rabusertib, SCH-900776, PF-477736, and AZD-7762. The plot to the right shows the selectivity of each compound (CATDS$_{CHEK1}$ at its K_d^{app}) as a function of drug concentration. AZD-7762 is a potent CHEK1 inhibitor but is not selective at any concentration. PF-477736 and SCH-900776 are selective at lower doses, and rabusertib is selective at all doses, because no other targets beside CHEK1 were observed in this screen. Further details are provided in figs. S3 and S4 and supplementary text.

a strict requirement for progressing compounds in the clinic (fig. S4, A and B). This is illustrated by the recent approval of midostaurin, a drug with a very broad kinase inhibitory profile. However, we argue that it is nonetheless important to determine the target spectrum of any drug that is administered to humans or used as a tool compound as carefully as possible to be able to make informed decisions in the clinic and in the research laboratory. The binding mode of KIs to kinases has been classified based on structural features. Analysis of 137 compounds with available binding mode information for the drug-kinase complex (fig. S4C) (*5*, *23*, *24*) confirmed that type 2 inhibitors (that is, KI binding to the inactive kinase conformation) are not necessarily more selective than type 1 inhibitors (that is, KI binding to the active kinase conformation; median CATDS of 0.4 versus 0.3) (*5*). Type 3 inhibitors showed a higher selectivity (median CATDS of 0.7), but these are special cases because most of them are designated MEK1/2 inhibitors that bind to a particular cavity adjacent to the ATP-binding site (*25*). Type 4 inhibitors bind to allosteric sites and usually do not score in the kinobeads assay unless binding leads to a conformational change involving the ATP-binding site (as observed for MK-2206). Irreversible KIs that target a cysteine residue in the ATP-binding site of EGFR (C797) or Bruton's tyrosine kinase (BTK) (C481) have received considerable attention (recent approvals of afatinib and ibrutinib, respectively). The nine irreversible EGFR and two BTK inhibitors in our panel showed a higher selectivity than reversible compounds (median CATDS of 0.6 and 0.4, respectively), but this was not universally the case. Most of the irreversible inhibitors bound both EGFR and BTK, albeit often with higher potency for the intended target. Some inhibitors can also reversibly bind kinases lacking the supposedly required cysteine residue (for example, pelitinib and WEE1). This may not be surprising because a kinase scaffold is still required to position the molecule at the intended target to permit irreversible binding. Additional experiments for 24 EGFR inhibitors (9 irreversible and 15 reversible) in the ERBB2-dependent breast cancer cell line BT-474 confirmed the results from the main kinobeads screen (fig. S4D). Even if selectivity cannot be universally claimed for these molecules, irreversible target binding increases the residence time of the drug, which can be useful for targeting long-lived proteins. Protein turnover measurements performed in HeLa cells confirmed that EGFR is a long-lived protein ($t_{1/2}$ = 271 hours; fig. S4E).

The drug-target data matrix can also be used in a target-centric fashion. For example, 19 drugs inhibited CHEK1 binding, many of which are not designated CHEK1 inhibitors. Although the designated CHEK1 inhibitor AZD-7762 was very potent (K_d^{app} of 5 nM), a low CATDS score at all concentrations showed that there are many other potent targets (Fig. 2B). Attributing cellular effects to the inhibition of CHEK1 would therefore often be difficult. Two other designated CHEK1 inhibitors, PF-477736 and SCH-900776, were similarly potent (K_d^{app} of 0.2 and 11 nM, respectively) but showed improved selectivity at concentrations of about 10 nM. Rabusertib was also similarly potent (K_d^{app} of 43 nM) but had no other targets in our assay. This drug is, by far, the most selective CHEK1 inhibitor in the panel tested and may therefore be the best current chemical probe for this protein. Another interesting and unexpected finding was that the target spectrum and potency of prodrugs and their active metabolites varied considerably (fig. S4F). Fasudil had many more targets than the active metabolite hydroxyfasudil (*14*). Conversely, the vascular endothelial growth factor receptor (VEGFR)/SRC prodrug TG-100801 had far fewer and less potent targets than the active drug TG-100572. The active metabolites of the SYK inhibitor fostamatinib and the Aurora drug barasertib had very different kinase binding profiles compared to the precursor molecules. All of the above shows that to understand the mechanisms by which a clinical drug exerts an effect in vivo, careful target deconvolution of the inhibitor, the formulation, and the metabolites should generally be performed.

Additional targets for established drugs

As expected, the vast majority of compounds interacted with protein/lipid kinases, but our study also revealed binding to seven metabolic kinases, 19 other nucleotide binders, five FAD (flavin adenine dinucleotide) binders, and the heme-binding enzyme FECH (ferrochelatase) (Fig. 3A and table S2). These unanticipated interactions not only may lead to desired consequences but also can represent mechanisms of drug toxicity. A survey of the scientific and patent literature (using PubMed, SciFinder, or ChEMBL) revealed that many of the 243 drugs investigated in this study are surprisingly poorly characterized with regard to their target space or bioactivities. At the time of writing, >110,000 publications were listed in PubMed, >90,000 publications and >47,000 patents in SciFinder, and >2400 bioactivities in ChEMBL (table S1). More than 50%

Downloaded from http://science.sciencemag.org/ on November 30, 2017

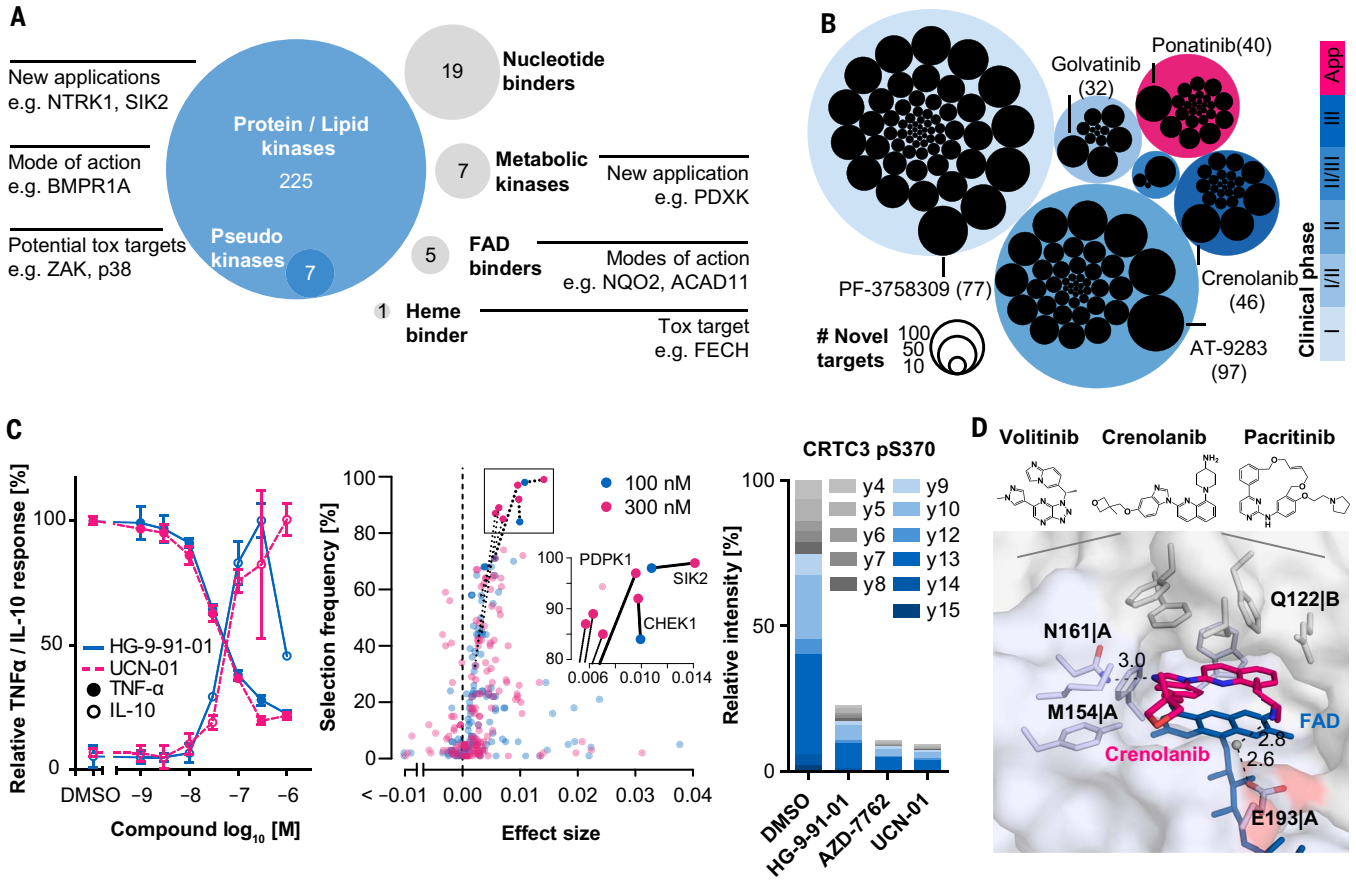

Fig. 3. Off-target interactions of KIs. (**A**) Target space of all 243 clinical KIs tested. Protein and lipid kinases plus several pseudokinases, metabolic kinases, FAD-binding proteins, and a heme-binding protein were identified as KI binders. Novel interactions may be exploited for new applications of a drug, to explain its mode of action, or to represent potential mechanisms of toxicity. (**B**) Number of novel targets for inhibitors grouped by clinical trial phase. Novel targets were determined for many compounds regardless of their clinical status. Each drug is shown as a black circle. The size of the circle is proportional to the number of targets not described in the literature or online databases (in brackets). (**C**) Validation of previously unidentified SIK2 inhibitors. Left panel: Treatment of lipopolysaccharide (LPS)–stimulated primary mouse bone marrow–derived macrophages (BMDMs) with the novel SIK2-binding drug UCN-01 led to a reduction in TNFα production and an increase of IL-10 secretion, indicating cellular activity of UCN-01. Error bars depict SD of three technical replicates. Middle panel: Elastic net analysis performed at two concentrations of TNFα-reducing compounds and control compounds without TNFα activity, but overlapping target profiles rank SIK2 as the top candidate responsible for the observed drug phenotype. Right panel: Quantitative PRM analysis showing a strong reduction of pS370 of CRTC3 (direct substrate of SIK2) in response to previously unidentified SIK2 inhibitors and confirming target engagement in primary BMDMs. (**D**) Cocrystal structure of NQO2 and crenolanib (pink) showing that the drug and cofactor (FAD, blue) simultaneously bind the active site of the nonkinase off-target NQO2 via π-stacking and contact to certain residues (sticks). The protein is shown as a semitransparent surface. The cocrystal structures of volitinib and pacritinib, as well as further details, are provided in figs. S5 to S7 and supplementary text.

of all publications in PubMed or SciFinder were covered by just five drugs (that is, rapamycin, imatinib, sorafenib, gefitinib, and erlotinib). Although structure-based searches identified patents for all compounds in SciFinder, 17 drugs had no PubMed entry at all (4 for SciFinder publications), 35 drugs had no listed bioactivity in ChEMBL, and 70 drugs had fewer than 10 publications in PubMed (50 such cases for SciFinder). This is very noteworthy because all of these molecules have been tested in humans. As a result, this study reports on a large number of novel molecular interactions and off-targets not previously covered by the scientific literature (Fig. 3B, fig. S5A, and table S7) (*6*, *11*, *12*, *26*). This includes clinically advanced compounds such as dabrafenib, a reportedly selective BRAF inhibitor. The kinobeads data showed that the drug is a multikinase inhibitor with ~30 submicromolar targets (fig. S5B). Kinase activity assays confirmed potent inhibition of several SRC family members, and there was no apparent difference in selectivity between the three RAF family members. Moreover, wild-type (WT) BRAF and the V600E mutation for which the drug is used in the treatment of melanoma were equally well inhibited (fig. S5, C to F). Our results also confirmed recent binding assay data (*27*) for the approved BCR-ABL inhibitor ponatinib. Far more potent targets were identified than previously described, and kinase assays validated potent inhibition of ZAK and MAPK14 (p38α) activity (fig. S5G). Both proteins are key regulators of the MAPK pathway, and inhibition thereof has been linked to desired and undesired effects. Notably, there are 16 submicromolar ZAK and 15 such p38α inhibitors in the panel of which 10 drugs cotarget ZAK and p38α. As a result, two nodes in the same essential pathway are inhibited, which may potentially lead to pleiotropic and unpredictable biological effects.

Polypharmacology also offers therapeutic opportunity, and our interaction screen provides many candidates for clinical reevaluation or as chemical starting points for the development of novel compounds. The early years of kinase drug discovery focused on very few kinases, but many more have come into focus in recent years (fig. S6A). One such protein is SIK2 (salt-inducible kinase 2), which is proposed as a target for inflammation and autoimmunity (*28*) because inhibition of SIK2 by dasatinib or the SIK tool compound HG-9-91-01

Downloaded from http://science.sciencemag.org/ on November 30, 2017

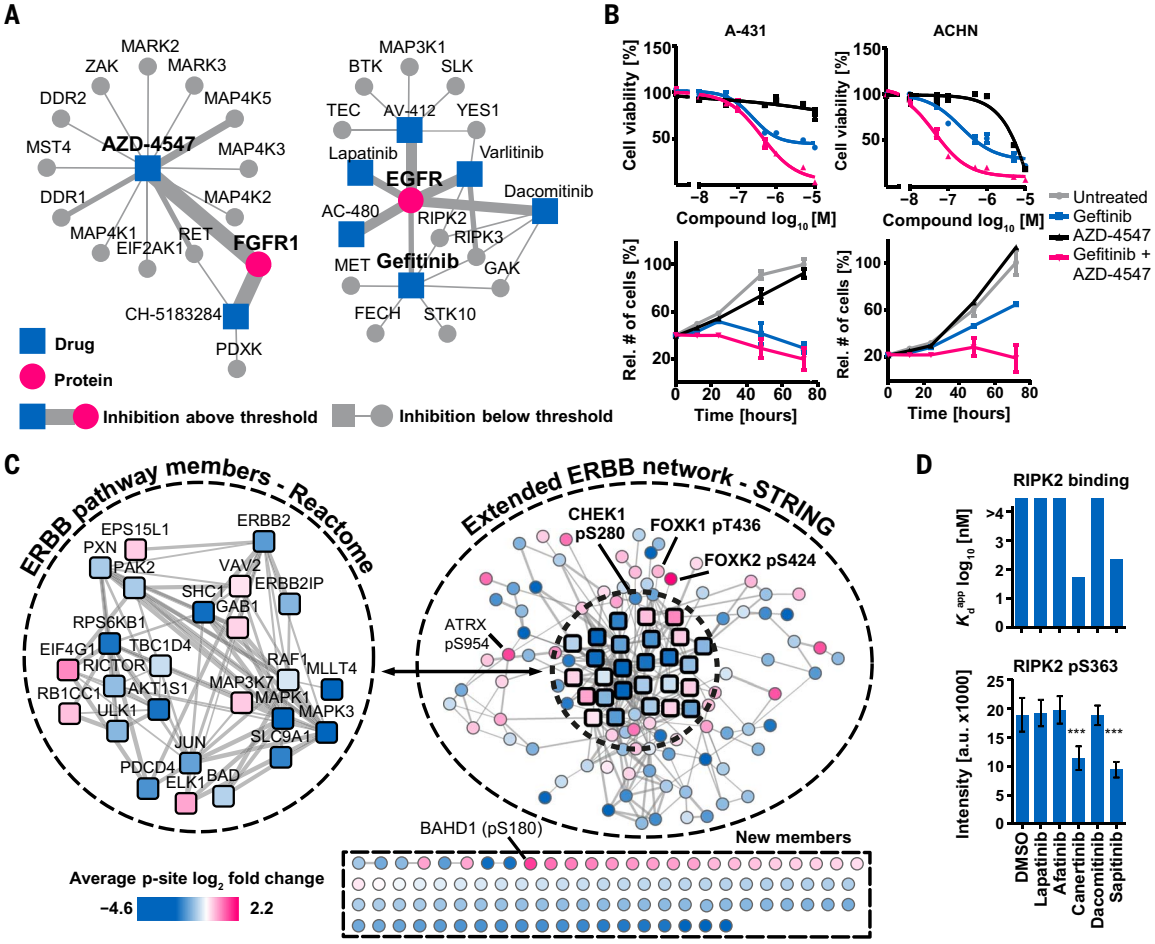

Fig. 4. Analysis from target to pathway engagement. (**A**) Visualization of protein-drug interactions in ProteomicsDB. Each node is a drug or a target, and the size of each edge is proportional to the pK_d^{app} of the interaction. Exploration of these networks can identify rational drug combinations to overcome drug resistance. (**B**) A-431 and ACHN cells that are partially sensitive to the EGFR inhibitor gefitinib were treated with gefitinib, the FGFR inhibitor AZD-4547, or a combination of both. Error bars depict SEM of three experiments. Cell viability and proliferation assays showed that the combination of the drugs was more effective than single compounds. (**C**) Quantitative phosphoproteomics was used to measure pathway engagement and identify common effects exerted by five KIs (lapatinib, afatinib, canertinib, dacomitinib, and sapitinib) in the ERBB2-driven breast cancer cell line BT-474. Numerous phosphorylation sites mapped to known ERBB pathway members (Reactome), and further proteins were associated with the ERBB network using STRING. Many further phosphorylation sites were consistently and statistically significantly regulated by the drugs ($P < 0.01$; scale: average $\log_2$ fold change across all inhibitors). These may represent previously unknown functional effector proteins or pathway biomarkers of EGFR signaling and drug response. (**D**) Conversely, using the phosphorylation status of pS363 of RIPK2 is not a reliable response marker for EGFR drugs, because phosphorylation abundance of this site was only reduced by two from five of the EGFR inhibitors (bottom panel, error bars depict SD) and instead only responded to inhibitors that are also RIPK2 inhibitors (top panel). Further details are provided in fig. S8 and supplementary text.

has been shown to reduce the production of the proinflammatory cytokine tumor necrosis factor–α (TNFα) and to up-regulate the secretion of the anti-inflammatory protein interleukin-10 (IL-10) in mouse bone marrow–derived macrophages (BMDMs) (*29*). Our kinobeads assays identified 21 SIK2 inhibitors with affinities of better than 500 nM, and we performed TNFα assays in murine BMDMs, showing that AZD-7762, BMS-690514, crenolanib, PF-03814736, and UCN-01 also suppressed LPS-induced TNFα production in a dose-dependent fashion (Fig. 3C, fig. S6B, and table S8). Further experiments on selected TNFα-reducing KIs in the same primary cell assay showed that the compounds also led to an increase of IL-10 production. Because all these inhibitors have additional targets, the TNFα phenotype may not only be attributable to the inhibition of SIK2. To test this, we performed elastic net analysis (*30*) on the SIK2 inhibitors and included eight further drugs that did not inhibit SIK2 and did not reduce TNFα production but have a large overlap in kinase targets with the SIK2 inhibitors. The results ranked SIK2 at the top of all candidates at nontoxic compound concentrations, indicating a very strong association of SIK2 inhibition and TNFα response (Fig. 3C; see supplementary text for further information). We next treated murine BMDMs with HG-9-91-01, dasatinib, AZD-7762, PF-03814735, UCN-01, and AT-9283 and quantified phosphorylation of pS62 and pS370 of CRTC3 (a direct substrate of SIK2) by parallel reaction monitoring (PRM) MS (Fig. 3C and fig. S6, C and D) (*31*, *32*). The data show that all six compounds led to a strong reduction of CRTC3 phosphorylation, demonstrating functional target engagement of the compounds in cells and lending further support to the interpretation that the observed TNFα and IL-10 responses are mediated by SIK2 inhibition.

Another emerging target is NTRK1 (TrkA) because NTRK1 fusion proteins have been identified as oncogenic drivers in lung, colon, and brain cancer (*33*–*35*). Our analysis identified 20 NTRK1 inhibitors, and viability assays in KM12 colorectal cancer cells (driven by TPM3-NTRK1) showed

Downloaded from http://science.sciencemag.org/ on November 30, 2017

that XL-228, foretinib, lestaurtinib, and TAK-901 were similarly potent as the designated NTRK1 inhibitor entrectinib (fig. S6F). Comprehensive target profiling can also improve understanding of the MoA of a KI. An example is the dual SRC/ABL inhibitor saracatinib that is undergoing clinical trials for bone cancer, among others. Proteins involved in bone morphogenesis, such as BMPR1A, ACVR1, and ACVR1B, were identified in our assay as high-affinity targets. In line with this hypothesis, the bone osteosarcoma cell line U-2 OS (high expression of BMPR1A) was more sensitive to saracatinib than the unrelated ovarian cancer cell line NCI/ADR-RES (low expression of BMPR1A). mRNA silencing in both cell lines showed that drug sensitivity was not exclusively due to SRC expression, suggesting that a proportion of the effect elicited by the drug is mediated by inhibition of bone morphogenetic protein (BMP) receptor signaling (fig. S6G). Further Western blot analysis revealed a dose-dependent decrease of SMAD1/5/9 phosphorylation (a downstream BMP effector) as well as SRC autophosphorylation. These data show that both SRC and the BMP receptors are engaged and required for cell viability, and thus suggest a dual mode of action of saracatinib in osteosarcoma cells (fig. S6, H and I; see supplementary text for further information).

In light of the above, we stress again that it is important to know the full target spectrum of a drug and that our resource fills an important gap in the scientific literature. In addition, the systematic identification of drug-target interactions could become a valuable tool for clinicians. In particular, the information assembled here and in ProteomicsDB may be of value to molecular tumor boards, where physicians and scientists seek to integrate clinical and molecular data to identify the best possible therapeutic regimen for an individual patient.

Less conventional targets of clinical KIs

Because the compounds immobilized on kinobeads are ATP mimetics, we and others have shown that other nucleotide-binding proteins may also specifically bind to them. The large body of data reported here expands on these previous observations. For example, the metabolic kinase PDXK has previously been shown to bind seliciclib (roscovitine) via the pyridoxal-binding site (*36*). We detected binding of PDXK to the designated PLK1 inhibitor BI-2536 (K_d^{app} = 387 nM), possibly via direct binding to the ATP site of PDXK (fig. S6J). Several KIs were potent binders of the acetyl–coenzyme A dehydrogenases ACAD10 (for example, alisertib) and ACAD11 (for example, crizotinib), which may be rationalized by binding to the FAD site of the enzymes (fig. S6K). Another member of the same enzyme superfamily is NQO2. This enzyme is potently inhibited by the BCR-ABL inhibitor imatinib (*13*). Our data revealed a further nine submicromolar binders of NQO2, most notably pacritinib (K_d^{app} = 4 nM) and crenolanib (K_d^{app} = 40 nM). Previous x-ray crystallography studies showed that imatinib binds to the FAD-binding site of the enzyme (*37*). Because the pharmacophores of some of the newly identified NQO2 binders are different to that of imatinib, we used x-ray crystallography to investigate the binding mode of crenolanib [Protein Data Bank (PDB) code, 5LBY], volitinib (PDB code, 5LBW), and pacritinib (PDB code, 5LBZ). The structures revealed that all compounds bound the FAD-binding pocket by π-stacking interactions with the isoalloxazine ring of the FAD molecule and also by specific interactions with N161, E193, or Q122 and M154 of the protein (Fig. 3D, fig. S6L, and supplementary text). Thus, NQO2 is a more common off-target of KIs than previously anticipated, but the physiological relevance of this interaction remains unclear. Recent reports have shown that KIs can bind the enzyme FECH and that inhibition of FECH is the mechanism by which the clinically observed photosensitivity of vemurafenib patients can be rationalized (*38*, *39*). This was surprising at the time, because the enzyme does not contain a nucleotide-binding site and subsequent biochemical assays showed that the inhibitors bind the protoporphyrin-binding site. The current profiling of 243 clinical drugs identified 4 additional FECH binders, increasing the total to 30 (fig. S6M), further supporting the notion that FECH assays should become part of preclinical KI testing.

Some kinases form relatively stable protein complexes, and some complexes are also enriched on kinobeads. Members of the AP2 complex that play a role in clathrin-mediated endocytosis were frequently observed (AAK1, AP2B1, AP2S1, and AP2M1). Other examples included inflammatory response–regulating complexes (TBK1, TBKBP1, AZI2, and TANK), the transfer RNA–modifying KEOPS complex (TP53K, TPRKB, OSGEP, and LAGE2), and other kinase interactors such as scaffolding proteins (INPPL1 and INCENP) and signaling modules [CSNK2A1/2 and EIF3J (*40*); LATS1 and MOB1; fig. S7, A and B]. CDK-cyclin complexes present an interesting case. On the basis of described functions in the regulation of the cell cycle (CDK1/2/4/5/6/7), transcription (CDK7/9/11/12), or other processes (atypical; CDK16/17/18), CDKs can be categorized into several cellular MoAs. Clustering of inhibitors that bind CDKs by CATDS score revealed that most of the designated CDK inhibitors were not very selective for any particular CDK, CDK complex, or cellular role (fig. S7, C and D). Conversely, several inhibitors, for which CDKs are off-targets, showed a preference for CDK complexes in the cell cycle, transcriptional, or atypical categories (fig. S7, C and E). In principle, this implies that it may be feasible to design CDK inhibitors in the future that are selective for one of these biological processes.

From target to pathway engagement

We have incorporated the present chemical proteomic data into ProteomicsDB (*15*) and added new functionality that displays the target spectrum and dose-response characteristics of each KI. This online resource also enables exploring potential drug combinations to overcome drug resistance (Fig. 4A). For example, it has been shown that growth factors secreted by the tumor microenvironment can lead to fibroblast growth factor receptor (FGFR)–mediated signaling that bypasses EGFR inhibition by gefitinib (*41*). ProteomicsDB can simultaneously visualize several target proteins and respective inhibitors thereof plus additional proteins targeted by these compounds. On the basis of this idea, the potent FGFR1 inhibitor AZD-4547 was chosen for combination treatments in four cell lines that are partially sensitive to gefitinib (A-431, skin, EGFR-WT; ACHN, kidney, EGFR-WT; IGROV-1, ovary, EGFR-WT; PC-9, lung, EGFR-activating E746-A750 deletion; Fig. 4B and fig. S8, A and B). Regardless of whether or not EGFR carried an activating mutation, the combination was always more effective in inhibiting cell viability and proliferation than any one drug alone.

One key challenge in drug discovery is to assess whether a drug molecule engages a target or associated pathway in a cell. The present resource allowed us to explore this in a novel way by analyzing the phosphoproteome of cancer cells in response to KI treatment and by integrating this information with the target spectrum of the drug(s) used. To illustrate this concept, the phosphoproteomes of BT-474 cells after treatment with the EGFR/HER2 inhibitors lapatinib, afatinib, canertinib, dacomitinib, and sapitinib were determined to a depth of ~15,000 phosphorylation sites (fig. S8C and table S9). The analysis revealed a surprisingly large number of statistically significantly regulated phosphorylation events for each drug (P < 0.01; minimum three from four replicates; fig. S8D). The five drugs have different selectivity in BT-474 cells (CATDS = 1.00, 0.78, 0.94, 0.77, and 0.73, respectively); thus, a common network affected by inhibition of the primary targets EGFR/HER2 was generated. Many of the 211 resultant proteins (274 regulated phosphorylation sites in at least four from five inhibitors) mapped to the EGFR/HER2 network (Fig. 4C) and can be functionally interpreted. For example, reduction of autophosphorylation on pY1248 from ERBB2 showed that the drugs are "on target" (fig. S8E). Diminished KRT8 phosphorylation (a substrate of EGFR) can be used as a target-proximal readout for reduced EGFR activity. Reduced phosphorylation of MAPK1 and MAPK3 (ERK1/2) confirmed the engagement of the MAPK signaling pathway in response to the drugs (fig. S8F). All five drugs led to the activation of CHEK1 (by reducing phosphorylation of the inhibitory site pS280, downstream of AKT), thus indicating activation of the DNA damage response pathway and protection from apoptosis (fig. S8G). Such observations not only uncover how the drug exerts its effects in cells but also can rationalize a combination treatment, for example, using the highly selective CHEK1 inhibitor rabusertib (see above). There are many proteins with significant changes in phosphorylation but without obvious connections to the EGFR/HER2 pathway (for example, transcription factors FOXK1 and FOXK2). Several of these sites or proteins have little or no ascribed function (supplementary text). However, the fact that such proteins consistently showed a robust response in cells to the EGFR inhibitors may imply that these are members of the network and

Downloaded from http://science.sciencemag.org/ on November 30, 2017

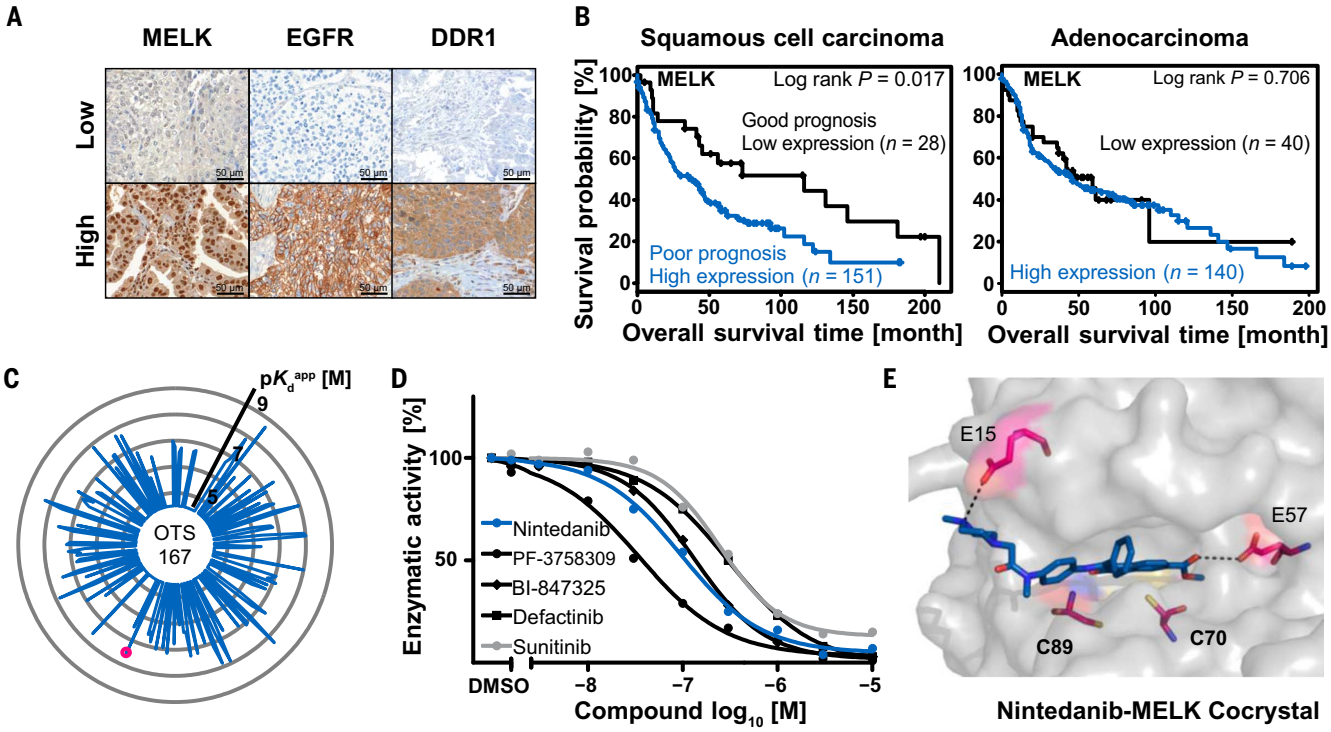

Fig. 5. Characterization of drugs targeting MELK. (**A**) Kinobeads profiling of 15 NSCLC patient tumors and adjacent healthy tissue identified overexpression of MELK, EGFR, and DDR1. Expression was confirmed by immunohistochemistry in a cohort of 375 NSCLC patients. (**B**) MELK overexpression correlated (log-rank test) with poor overall survival in SCC but not ADC patients. (**C**) Radar plot depicting targets and binding affinities of the phase 1 MELK inhibitor OTS-167 (each spoke is a direct binder, and the length of the spoke is indicative of binding affinity), showing that the drug is a very unselective compound and suggesting that its biological activities may not be due to MELK inhibition alone. MELK is marked by a red dot. (**D**) Kinase activity assays confirmed that MELK binders identified in this study (for example, nintedanib) are also potent MELK inhibitors. (**E**) Cocrystal structures obtained for five MELK inhibitors revealed that nintedanib forms strong interactions with residues E15 and E57 in the ATP pocket. There are additional residues (notably, C70 and C89) that may be exploited to develop selective and potent irreversible MELK inhibitors. Further details are provided in fig. S9 and supplementary text.

may act as response markers of drug action. To assess the molecular consequences of polypharmacology, comparative phosphorylation signatures of individual drugs are also valuable. For example, RIPK2 has recently been implicated as a target in breast cancer (*42*). In addition to EGFR, kinobeads profiling showed that although canertinib and sapitinib are potent inhibitors of RIPK2, lapatinib, afatinib, and dacomitinib are not. Consequently, RIPK2 pS363 levels in BT-474 cells were only reduced by canertinib and sapitinib. Thus, this site is a target engagement marker for drugs specific for RIPK2 but not EGFR (Fig. 4D). Again, the above analysis highlights the need to thoroughly profile the target space of any KI to understand its cellular MoA.

Initial drugs for potential novel kinase targets

One use case of the drug-target matrix provided by this study is to identify compounds with very good drug-like properties for potential novel targets. These drugs may serve as high-value chemical leads to inform or jump-start a drug discovery program. To illustrate this concept, expression profiling using kinobeads was performed on 15 non–small cell lung cancer (NSCLC) tumors and adjacent healthy tissue from the same patients (fig. S9A and table S10). Among the overexpressed kinases in tumors were the well-known drug targets EGFR and MAP2K1 (MEK1), as well as the kinases DDR1 and MELK (maternal embryonic leucine zipper kinase). A retrospective survival analysis of a cohort of 375 NSCLC patients was performed by staining tissue microarrays (TMAs) for EGFR, DDR1, and MELK (Fig. 5, A and B; fig. S9, B to D; and supplementary text). The combined analysis of squamous cell carcinoma (SCC) and adenocarcinoma (ADC) cases showed no significant correlation with EGFR and DDR1 expression and a moderate effect for MELK (log-rank test, $P = 0.04$). However, separate analysis of SCC and ADC showed that high MELK expression was more strongly correlated with poor survival in SCC but not ADC patients ($P = 0.02$ versus $P = 0.71$). These results confirmed earlier reports that MELK is a potential predictive marker for poor prognosis in SCC-NSCLC (*43*). Given this differential expression pattern and the fact that MELK is a kinase, the protein may have potential as an actionable target in the SCC-NSCLC subtype of lung cancer. There is some controversy about the validity of MELK as a target because recent work in cell lines has shown that the protein is not generally required for the growth of cancer cells (*44*, *45*). In these studies, neither pharmacological inhibition nor CRISPR-Cas9–mediated knockout of the protein showed a growth-inhibiting phenotype. However, as these authors also point out, the current data cannot rule out the possibility that MELK, or mutants thereof, may play important roles in vivo, for example, in tumor maintenance. Therefore, we emphasize that our observations do not specifically provide validation for MELK as an oncology target but serve to illustrate how our drug-target interaction screen might be used to inform a preclinical drug discovery project.

The only designated MELK inhibitor currently in clinical trials is OTS-167 (phase 1). Kinobeads profiling for this drug showed that it is a very broad multikinase inhibitor and will thus likely not contribute to the clinical validation of MELK as a drug target (Fig. 5C). Moreover, its efficacy in cancer cells may actually not stem from the inhibition of MELK. A further 16 MELK inhibitors were identified in our present work (including the approved drugs nintedanib and sunitinib) and kinase activity assays confirmed reasonably potent enzymatic inhibition (Fig. 5D). To gain insight into the structure-activity relationship of MELK inhibitors, the protein was cocrystallized

Downloaded from http://science.sciencemag.org/ on November 30, 2017

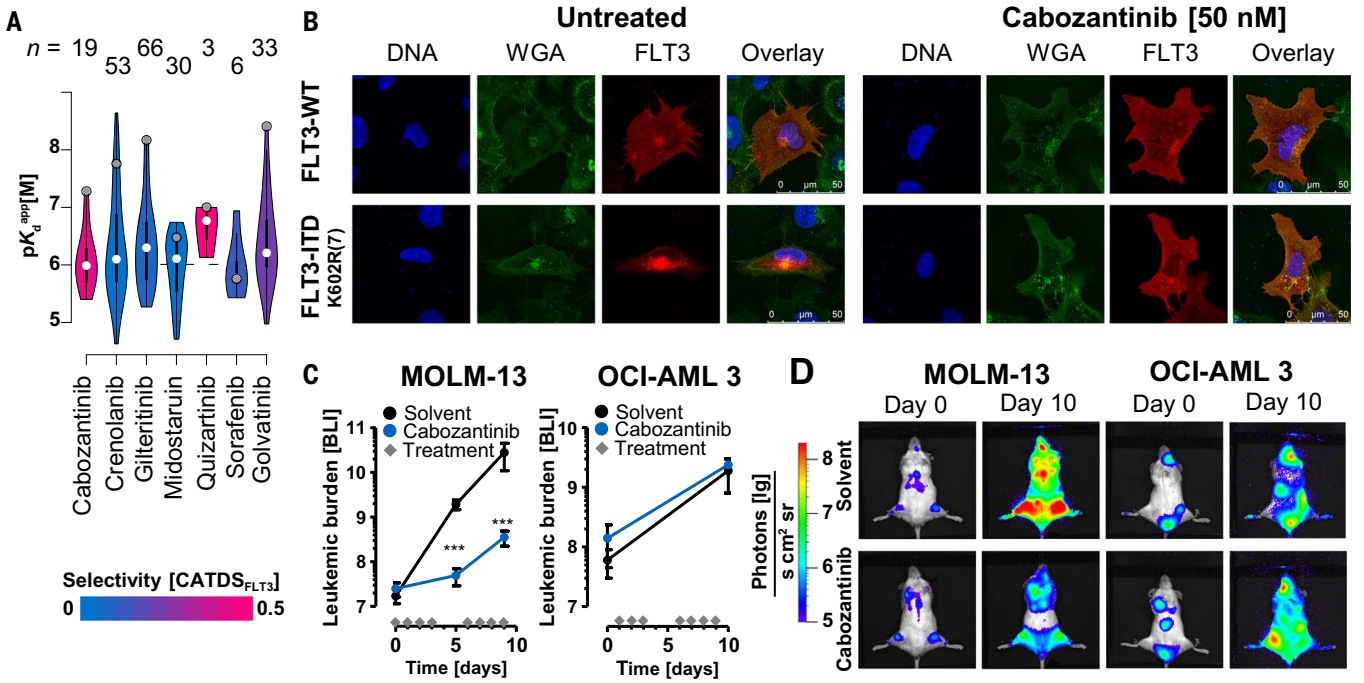

Fig. 6. Repurposing of cabozantinib for the treatment of FLT3-ITD–positive AML. (**A**) Violin plots comparing the potency and selectivity of some FLT3 inhibitors identified in this study (figures at the top indicate the number of targets of the respective compound). (**B**) Immunofluorescence staining of U-2 OS cells expressing FLT3-WT or the FLT3-ITD K602R(7) mutant protein. Staining for DNA (DAPI, blue), membrane structures (WGA, green), and FLT3 (red) showed that FLT3-WT predominantly localized to the plasma membrane, whereas the mutant protein accumulated in the perinuclear endoplasmic reticulum. Cabozantinib treatment had no effect on FLT3-WT localization. FLT3-ITD localization to the plasma membrane was restored, analogous to the cellular phenotype of the WT protein. (**C**) Measurement of tumor burden by bioluminescence [photons (lg)/(s*cm^2*sr)] in cabozantinib (blue, n = 6) or vehicle-treated mice (black, n = 5) xenografted with MOLM-13 (FLT3-ITD) or OCI-AML3 (FLT3-WT) cells. Diamonds on the x axis indicate days of drug treatment; error bars depict the SD in the aforementioned groups of animals. Proliferation of MOLM-13 cells in cabozantinib-treated animals was significantly slowed compared to vehicle control (day 5, P = 0.00003; day 10, P = 0.00013, unpaired t test). No such effect was observed for animals xenografted with OCI-AML3 cells. Thus, cabozantinib specifically inhibited FLT3-ITD but not FLT3-WT AML cells in vivo. (**D**) Representative whole-animal bioluminescence imaging of MOLM-13 (FLT3-ITD) and OCI-AML3 (FLT3-WT) xenografts on days 0 and 10 after cabozantinib treatment, showing that the drug slows the proliferation of AML cells in vivo. Further details are provided in fig. S10 and supplementary text.

with nintedanib (PDB code, 5MAF), K-252a (PDB code, 5M5A), defactinib (PDB code, 5MAH), PF-3758309 (PDB code, 5MAG), and BI-847325 (PDB code, 5MAI). Not only are these the first MELK structures with clinical KIs, but also the analysis revealed 10 amino acids within the ATP pocket that may be particularly suitable for the development of selective and potent MELK inhibitors (fig. S9E) (*46*). Specifically, nintedanib engaged in two drug-protein interactions not observed with the other structures (E15, selectivity residue; E57, potency residue). In addition, the structure revealed two readily accessible cysteine residues (C70 and C89) that only exist in 1% of all human kinases and that could therefore be used for the design of irreversible MELK inhibitors with improved selectivity (Fig. 5E, fig. S9E, table S11, and supplementary text). In our view, the above is a clear example for how drug repositioning or medicinal chemistry can be conceptually approached using systematic profiling data of clinical compounds.

Repurposing cabozantinib for treatment of FLT3-positive acute myeloid leukemia

The discovery that the BCR-ABL inhibitor imatinib also potently inhibits c-KIT and platelet-derived growth factor receptor (PDGFR) mutations extended the use of this drug from chronic myelogenous leukemia to the treatment of gastrointestinal stroma tumors (*47*). It also demonstrated that KI polypharmacology can be exploited to repurpose compounds for other indications. The KI interaction study provided here should enable the scientific community to discover such opportunities more systematically. As an example, the kinobeads data (Fig. 6A) revealed that the designated MET/VEGFR inhibitors cabozantinib (approved for the treatment of medullary thyroid cancer and advanced renal cell carcinoma) (*48*) and golvatinib, among others, are potent inhibitors of the mutated tyrosine kinase FLT3-ITD that is involved in an aggressive form of acute myeloid leukemia (AML). This potential FLT3 activity was not previously known for golvatinib. Both compounds killed FLT3-ITD–dependent tumor cells, and Western blot analysis showed that both compounds abrogated FLT3 autophosphorylation, thus demonstrating target engagement in cells (fig. S10, A to D). Because cabozantinib is an already approved drug, we performed further experiments to assess whether cabozantinib may be repurposed to treat FLT3-ITD–dependent AML. To this end, a panel of AML cell lines was treated with cabozantinib and the FLT3 inhibitors quizartinib and crenolanib. The FLT3 mutant cell lines (MV-4-11, MOLM-13, and MONO-MAC-6) were sensitive to all three drugs; however, FLT3-WT cells (OCI-AML3, HL-60, KG-1a, and THP-1) did not respond. Additional experiments in murine Ba/F3 cells harboring FLT3-ITD mutations showed potent inhibition by the three inhibitors of most, but not all, mutants (fig. S10, A and B, and supplementary text). Immunofluorescence experiments showed that the FLT3-WT protein prominently localized to the plasma membrane, but FLT3-ITD K602R(7) or FLT3-ITD E611C(28) U-2 OS cells showed localization primarily in the cytosol. Cabozantinib treatment restored the cellular distribution to that of the WT protein (Fig. 6B and fig. S10E). Immunoblotting revealed that low nanomolar concentrations of cabozantinib also abrogated signal transducer and activator of transcription 5 (STAT5) phosphorylation downstream of FLT3 in MV-4-11 cells, thus indicating that the drug has a similar inhibitory effect as quizartinib on aberrant FLT3-ITD signaling in AML cells (fig. S10D) (*49*). To assess the in vivo efficacy of cabozantinib, mice were xenografted with MOLM-13

Downloaded from http://science.sciencemag.org/ on November 30, 2017

(FLT3-ITD; $n = 6$) or OCI-AML3 (FLT3-WT; $n = 5$) cells and treated with cabozantinib. Bioluminescence measurements revealed that the tumor burden of treated mice injected with FLT3 mutant cells was significantly reduced upon cabozantinib treatment compared to the untreated control. FLT3-WT xenografts showed no difference in tumor burden between drug or vehicle treatment (Fig. 6, C and D). To monitor survival, drug dosing was stopped on day 14 after cell injection and the last animal was sacrificed on day 26. Cabozantinib significantly reduced tumor growth in FLT3-ITD AML cells in vivo, and Kaplan-Meier analysis showed a statistically significant, positive effect on survival in the drug-treated animals ($P = 0.01$; fig. S10, F to H). Collectively, these preclinical data and recent similar results (50) are in support of initiating a phase 2 clinical trial of cabozantinib in FLT3-ITD–stratified AML patients. We believe that this is an innovative approach, because cabozantinib is as potent and selective as quizartinib but more potent and selective than midostaurin (Fig. 6A), which was recently approved for the treatment of AML.

Our interactive ProteomicsDB database provides a rich open-access resource to study the molecular landscape of clinically evaluated small-molecule KIs and targets. We highlight examples for why this information is important and how it may be used. The demonstration that repurposing kinase drugs is feasible and can be approached in a systematic fashion is a timely message. To promote and facilitate further exploitation of the data, we provide extensive new functionality in ProteomicsDB and ready-to-use target summaries for each of the 243 drugs. The data can be queried by a purpose-built shinyApp to ask specific questions about selectivity and binding affinity for drugs and targets of interest. We are committed to keeping this resource up to date and anticipate that engaging the community in the project will improve our understanding on the MoA of cancer drugs, facilitate the design of innovative clinical trials, foster the development of novel compounds, and aid molecular tumor boards in clinical decision-making.

Materials and methods

Cell lines, affinity matrices, and reagents for kinase inhibitor profiling

The cell lysate mixture (cell line mix) used to profile all kinase inhibitors in this study was generated from K-562, COLO 205 and MV-4-11 cells grown in RPMI 1640 medium (Biochrom GmbH), SK-N-BE(2) cultured in DMEM/HAM's F-12 medium (Biochrom GmbH). All were supplemented with 10% FBS (Biochrom GmbH) and 1% antibiotic solution (Sigma). Cell lines were authenticated by multiplex human cell line authentication test (MCA) and tested internally for mycoplasma contamination. For MET-inhibitor profiling, Caki-1 cells were cultured in IMDM (Biorad) with 10% FBS. For EGFR-inhibitor profiling, BT-474 cells were grown in DMEM/HAM's F-12 supplemented with 15% FBS (Biochrom). Kinase inhibitor affinity matrices (kinobeads) were synthesized in house as published (14). Omipalisib with a linker was internally synthesized. Small molecule kinase and other inhibitors were purchased from Selleckchem, MedChemExpress, Active Biochem, Abmole, Merck, or LC Laboratories (table S1).

Kinase inhibitor profiling with affinity matrices (Kinobead pulldowns)

Kinobead pulldown assays were performed as previously described (14). Briefly, cells were lysed in 0.8% NP40, 50 mM Tris-HCl pH 7.5, 5% glycerol, 1.5 mM MgCl2, 150 mM NaCl, 1 mM Na3VO4, 25 mM NaF, 1 mM DTT and supplemented with protease inhibitors (SigmaFast, Sigma) and phosphatase inhibitors. The protein concentration was adjusted to 5 mg/mL. Kinase inhibitors of interest were spiked into 1 mL lysate at increasing concentrations (DMSO vehicle, 3 nM, 10 nM, 30 nM, 100 nM, 300 nM, 1 μM, 3 μM and 30 μM) and incubated for 45 min at 4°C. This was followed by incubation with kinobeads (35 μL settled beads) for 30 min at 4°C. To assess the degree of protein depletion from the lysates by the kinobeads, a second Kinobead pulldown (with fresh beads) was performed on the unbound fraction of the vehicle control (so-called pulldown of pulldown). This enabled the determination of a correction factor for each protein that was used to calculate apparent dissociation constants for a drug-target complex. Proteins bound to kinobeads were eluted with LDS sample buffer (NuPAGE, Invitrogen) containing 50 mM DTT and stored until required. The same procedure was used for immobilized omipalisib (coupling density 1 μmol/mL).

Western blotting of kinobeads eluates was performed using the following antibodies: SIK2 (sc-393139 (B-12), Santa Cruz Biotechnology), PAK4 (#3242, Cell Signaling Technology), CHEK1 (#2360, Cell Signaling Technology), α-tubulin (sc-12462-R (E-19), Santa Cruz Biotechnology).

Liquid chromatography–tandem mass spectrometry (LC-MS/MS)

Kinobeads eluates were alkylated with chloroacetamide (55 mM) and run into a 4-12% NuPAGE gel (Invitrogen; approximately 1 cm). In-gel digestion was performed according to standard procedures. Generated peptides were analyzed by LC-MS/MS on a nanoLC-Ultra 1D+ (Eksigent) coupled to an LTQ Orbitrap Elite mass spectrometer (Thermo Fisher Scientific). Peptides were delivered to a trap column (75 μm × 2 cm, self-packed with Reprosil-Pur C18 ODS-3 5 μm resin, Dr. Maisch, Ammerbuch) at a flow rate of 5 μL/min in solvent A0 (0.1% formic acid in water). Peptides were separated on an analytical column (75 μm × 40 cm, self-packed with Reprosil-Gold C18, 3 μm resin, Dr. Maisch, Ammerbuch) using a 100 min linear gradient from 4-32% solvent B (0.1% formic acid, 5% DMSO in acetonitrile) and solvent A1 (0.1% formic acid, 5% DMSO in water) at a flow rate of 300 nL/min (51). The mass spectrometer was operated in data dependent mode, automatically switching between MS and MS2 spectra. MS1 spectra were acquired over a mass-to-charge (m/z) range of 360-1300 m/z at a resolution of 30,000 (at m/z 400) in the Orbitrap using an automatic gain control (AGC) target value of 1e6 or maximum injection time of 100 ms. Up to 15 peptide precursors were selected for fragmentation by higher energy collision-induced dissociation (HCD; isolation width of 2 Th, maximum injection time of 100 ms, AGC value of 2e5) using 30% normalized collision energy (NCE) and analyzed in the Orbitrap (7,500 resolution). A previous experimentally-obtained inclusion list containing approximately 1,000 kinase peptide m/z and retention time values was enabled in the data acquisition regime. Dynamic exclusion was 20 s and singly-charged precursors were excluded. Profiles of EGFR inhibitors in BT-474 cells were obtained using a Dionex Ultimate 3000 nano HPLC coupled to a Q Exactive HF mass spectrometer. Experiments using the immobilized omipalisib probe were analyzed on a nanoLC-Ultra 1D+ coupled to a Q Exactive HF mass spectrometer. For both instruments, peptides were delivered to a trap column as described above and separated on an analytical column using a 60 min gradient from 4-32% solvent B in solvent A1. MS1 spectra were acquired at a resolution of 60,000 (at m/z 200) using a maximum injection time of 10 ms and an AGC target value of 3e6. Up to 12 peptide precursors were isolated (isolation width of 1.7 Th, maximum injection time of 75 ms, AGC value of 2e5) and fragmented by HCD using 25% NCE and analyzed at a resolution of 15,000. Precursor ions that were singly-charged, unassigned or with charge states >6+ were excluded. The dynamic exclusion duration of fragmented precursor ions was 30 s.

Peptide and protein identification and quantification

Peptide and protein identification plus quantification were performed with MaxQuant (version 1.5.3.30.) (52) by searching the MS2 data against all canonical protein sequences as annotated in the Swissprot reference database (human proteins only, 20,193 entries, downloaded 22.03.2016, internally annotated with PFAM domains) using the embedded search engine Andromeda (53). Carbamidomethylated cysteine was a fixed modification; and phosphorylation of serine, threonine, and tyrosine, oxidation of methionine, and N-terminal protein acetylation were variable modifications. Trypsin/P was specified as the proteolytic enzyme and up to two missed cleavage sites were allowed. Precursor and fragment ion tolerances were 10 ppm and 20 ppm, respectively. Label-free quantification (54) and data matching between consecutive analyses were enabled within MaxQuant. Search results were filtered for a minimum peptide length of seven amino acids, 1% peptide and protein FDR plus common contaminants and reverse identifications. For consistent peptide identification and protein grouping, the MS data for each compound was supplemented with 15 standard DMSO controls. Each compound was analyzed separately.

Data analysis

For the kinobeads competition binding assays, protein intensities were normalized to the respective DMSO control and IC_{50} and EC_{50} values

Downloaded from http://science.sciencemag.org/ on November 30, 2017

were deduced by a four-parameter log-logistic regression using an internal pipeline that utilizes the 'drc' (55) package in R. A K_d^{app} was calculated by multiplying the estimated EC_{50} with a protein-dependent correction factor (depletion factor) that was limited to a maximum value of 1. The correction factor (cf) for a protein is defined as the ratio of the amount of protein captured from two consecutive pulldowns of the same DMSO control lysate (14, 56). In this study, protein-dependent correction factors were set to the median of correction factors across all experiments using the same lysate and beads.

mRNA sequencing

Total RNA from the cell lines COLO 205, K-562, MV-4-11 and SK-N-BE(2) was isolated using the RNeasy Plus Kit (Qiagen). Concentrations of purified RNA were determined using the Qubit 2.0 Fluorometer (Thermo Fischer Scientific) and the integrity was assessed applying the Agilent 2100 Bioanalyzer (Agilent). A RIN value of 10 indicated maximum integrity for all four cell line samples. TruSeq RNA Sample Preparation Kit V2 (Illumina) was subsequently used for library synthesis according to the manufacturer's instructions. 10 nM of normalized libraries were pooled and loaded onto the flow cell of a HiSeq2500 Sequencing System (Illumina), followed by cluster generation and sequencing-by-synthesis. Samples were sequenced to a depth ranging from 51,583,423 (MV-4-11) to 63,500,730 purity filtered paired end reads (SK-N-BE (2)) of 101 bp length. Raw sequence data were mapped to the hg37 reference genome and processed to determine transcript expression and variants using Genomatix Mining station, NGSAnalyzer (Genomatix Software GmbH, Munich, Germany) and Integrative Genomics Viewer (57, 58).

Deep proteome profiling of cell lines

Proteins were extracted and concomitantly reduced and alkylated using lysis buffer (50 mM Tris-HCl pH 7.6, 8 M urea, 10 mM Tris-(2-carboxyethyl)-phosphin-HCl, 40 mM chloro-acetamide, protease inhibitor SigmaFast (S8820-20TAB) and Phosphatase inhibitor cocktail). Protein concentration of the cell extract was determined using a Bradford assay (Thermo Fisher Scientific). A total of 300 μg protein extract was diluted with digestion buffer (50 mM Tris-HCl pH 7.6) to reduce the urea concentration to <1.6 M, and subsequently digested with trypsin (1:100 protease: protein ratio). After a pre-digestion step (4 hours, 37°C), another aliquot of trypsin was added (1:100 protease:protein ratio), and the sample was further incubated overnight at 37°C. The tryptic digest was acidified with formic acid (final concentration 1% v/v), precipitates were removed by centrifugation (14,000 x g, 4°C, 10 min), the supernatant was desalted and concentrated using C18 Sep-Pak columns according to the manufacturer's instructions (Waters), and dried down in a vacuum centrifuge. The desalted digest was resolubilized in 5 mM Tris, pH 8.5 prior to hydrophilic SAX (hSAX) chromatography as described before (59). Thirty-six hSAX fractions were collected and desalted using C18 StageTips as described (60). Each desalted peptide pool was analyzed by LC-MS/MS as follows. Desalted peptide samples (10% of each hSAX fraction) were analyzed on a LC-MS/MS system consisting of an Eksigent NanoLC415 (Eksigent) ultrahigh pressure nano LC system coupled online to a Q Exactive Plus mass spectrometer (Thermo Scientific). Peptides were first delivered to a trap column (100 μm x 2 cm, packed in house with Reprosil-Pur C18 ODS-3 5 μm resin, Dr. Maisch, Ammerbuch) at a flow rate of 5 μL/min in solvent A0 (0.1% formic acid in water). Peptides were separated on an analytical column (75 μm x 40 cm, packed in-house with Reprosil-Gold C18, 3 μm resin, Dr. Maisch, Ammerbuch) using a 100 min linear gradient from 4-32% of solvent B (0.1% formic acid, 5% DMSO in acetonitrile) and solvent A1 (0.1% formic acid, 5% DMSO in water) at a flow rate of 300 nL/min (51). Full scan MS1 spectra were acquired at a resolution of 70,000 (at m/z 200) in the Orbitrap using a maximum injection time of 100 ms and an AGC target value of 3e6. Up to 20 peptide precursors were sequentially selected and subjected to fragmentation by HCD using 25% NCE (isolation width of 1.7 Th, maximum injection time of 50 ms, AGC value of 1e5, 17,500 resolution). Dynamic exclusion duration of fragmented precursor ions was set to 20 s. Peptide and protein identification and quantification was performed using MaxQuant (version 1.5.3.30) as described above. Absolute quantification using iBAQ was enabled.

Kinase activity assays

Kinase activity assays were performed at Reaction Biology Corp. or ProQinase GmbH. IC_{50} values were obtained using 10 drug concentrations in semi-log steps. Kinases of interest were measured at an ATP concentration corresponding to the apparent K_m for ATP of the corresponding kinase.

Pulsed SILAC experiments for EGFR half-life determination

HeLa cells were cultured in SILAC DMEM (Thermo Fisher Scientific) supplemented with 10% dialyzed FBS (GibcoTM), 1% antibiotic antimycotic solution (Sigma) and 1.74 mM L-proline (≥99%, Sigma). Arginine and lysine were added in either light (K0, isotope purity ≥99%; R0, ≥98%, Sigma) or heavy (K8, ≥99%; R10, ≥99% Cambridge Isotope Laboratories) form to a final concentration of 0.798 mM for lysine and 0.398 mM for arginine. After 10 cell doublings in heavy medium, proteins were tested for label incorporation (>99% K8 and R10). For the pulse experiment, heavy medium was replaced with light medium after washing the cells twice using sterile PBS. HeLa cell doubling time was determined by cell counting (six replicates every 12 h). Cells were lysed at 1, 3, 6, 10, 16, 24, 34 and 48 h after the medium switch using 8M urea in 40 mM Tris-HCl containing 1x protease inhibitor (cOmplete™, Mini, EDTA-free Protease Inhibitor Cocktail Tablets, Roche) and 1x phosphatase inhibitors. Lysates were cleared by centrifugation for 30 min at 20,000 g and 4°C and protein concentration was determined by the Bradford method (Coomassie (Bradford) Protein Assay Kit, Thermo Fisher Scientific).

After reduction (10 mM DTT, 30°C, 30 min) and alkylation (50 mM chloroacetamide, room temperature, 30 min, in the dark), the lysate was diluted to 1.6 M urea using 40 mM Tris-HCl. Digestion was performed using trypsin (Promega, 1:50 enzyme-to-substrate ratio) and incubating overnight at 37°C at 700 rpm on a thermoshaker. Digests were acidified by addition of neat formic acid (FA) to 1% and desalted by centrifugation through self-packed Stage Tips (loading and wash solvent: 0.1% FA; elution solvent: 0.1% FA, 60% acetonitrile). For this, 200 μl pipette tips were packed with five C18 extraction disks (Ø 1.5 mm, 3M EmporeTM SPE disks, Sigma-Aldrich) and fixed in the cut lids of 1.5 mL tubes. The material was washed and activated using 250 μL acetonitrile and 250 μL elution solvent, then equilibrated applying 500 μL wash solvent. Next, samples were slowly loaded twice, washed with 250 μL wash solvent and eluted using 50 μL elution solvent. Peptide solutions were frozen and dried in a SpeedVac.

High-pH reversed-phase tip fractionation was also performed in Stage Tips, constructed as described above. Tips were washed using 250 μL of 100% ACN, followed by 250 μL of 60% ACN in 25 mM NH_4COOH, pH 10 and then equilibrated with 500 μL of 25 mM NH_4COOH, pH 10. Subsequently, the desalted peptides were reconstituted in 50 μL of 25 mM NH_4COOH, pH 10, and slowly loaded onto the C18 material. After reapplication of the flow through, bound peptides were eluted using 40 μL of solvent with increasing concentrations of ACN (5, 10, 15, 17.5, 50% ACN) in 25 mM NH_4COOH, pH 10. The 5 and 50% ACN fractions were pooled and the 17.5% ACN fraction was combined with the previously stored flow through, resulting in a total of four fractions, which were dried and stored at −20°C until LC-MS/MS measurement.

Nanoflow LC-ESI-MS/MS measurements were performed with a Dionex Ultimate 3000 UHPLC+ system coupled to a Fusion Lumos Tribrid mass spectrometer (Thermo Fisher Scientific). After reconstitution in 1% FA, 1/6th of each high pH-RP fraction was injected. Peptides were delivered to a trap column (75 um x 2 cm, packed in-house with 5 μm C18 resin; Reprosil PUR AQ, Dr. Maisch) and washed using 0.1% formic acid at a flow rate of 5 μL/min for 10 min. Subsequently, peptides were transferred to an analytical column (75 um x 45 cm, packed in-house with 3 μm C18 resin; Reprosil Gold, Dr. Maisch) applying a flow rate of 300 nL/min and separated using a 100 min linear gradient from 4% to 32% LC solvent B (0.1% FA, 5% DMSO in ACN) in LC solvent A (0.1% FA in 5% DMSO). The mass spectrometer was operated in positive ionization mode. Full scan MS1 spectra were recorded from 360 to 1300 m/z at a resolution of 60,000 (at m/z 200) using an AGC target value of 4e5 charges and a maximum injection time of 50 ms. Up to 15 sequentially selected precursors (isolation window

Downloaded from http://science.sciencemag.org/ on November 30, 2017

1.6 m/z) were fragmented via HCD using a normalized collision energy of 28%. MS2 spectra were recorded at a resolution of 15,000 using an AGC target value of 1e5 and a maximum injection time of 100 ms. Fixed first mass and dynamic exclusion were set to 100 m/z and 60 s, respectively.

Peptide and protein identification and quantification was performed using MaxQuant (version 1.5.5.1). Raw files were searched against the UniProtKB database (human, 42,145 entries, downloaded 01.02.2016) with K0/R0 and K8/R10 specified as metabolic labels. Carbamidomethylated cysteine was set as fixed modification and oxidation of methionine, and N-terminal protein acetylation as variable modifications. Trypsin/P was specified as the proteolytic enzyme, with up to two missed cleavage sites allowed. Precursor tolerance was set to ±5 ppm, and fragment ion tolerance to ±20 ppm. Results were adjusted to 1% PSM and 1% protein FDR.

For half-life determination, fractions of heavy EGFR peptides (summed intensities of heavy peptides divided by summed intensities of light and heavy peptides) were plotted over time and a curve was fitted following a one phase decay equation:

$$f(t) = (A - B)e^{-Kt} - B \quad (1)$$

where K is the rate constant of the decay of heavy label, A is the fraction of heavy label at t=0 and B the fraction of heavy label at t=inf.

As the decrease of heavy label is affected by the half-life of the protein as well as the cell growth, K can be formulated as:

$$K = k_d + k_{cd} \quad (2)$$

where k_d is the protein degradation rate constant and k_{cd} is the rate constant of the cell doubling. The latter was obtained by fitting an exponential growth equation to the cell counts determined over the course of the pulsed SILAC experiment. The protein half-life $T_{½}$ can then be calculated as:

$$T_{½} = \frac{ln2}{k_d} \quad (3)$$

Comparison of kinase inhibitor profiles/targets to other published data

For the purpose of this comparison, only targets annotated as either direct Kinobead binders or kinases were considered in the comparison to interactions reported in the literature or major online databases. Datasets obtained from CHEMBL, LINCS, Anastassiadis *et al.* (*6*) and Metz *et al.* (*11*) were filtered for compounds used in the Kinobead drug screen and protein names were annotated according to gene names as used in UniProt. Dose response data was filtered for half maximal response at 30 μM or lower if the assay threshold concentration was lower. Single concentration data was filtered for a minimum of 25% inhibition of binding or activity.

Analysis of scientific literature on kinase inhibitors (as of June 2017)

The number of PubMed entries was derived from searching the kinase inhibitor and its synonyms in the PubMed database. This analysis includes primary scientific literature as well as reviews and published clinical trial reports about the respective drug. Additionally, the kinase inhibitors (using their respective CHEMBL IDs) were also searched for scientific literature reporting any type of bioactivities (e.g. data on single proteins, cell lines, organisms) in the CHEMBL database. A structure search was performed in SciFinder and yielded the overall number of publications and patents annotated to this compound structure (including reviews).

Cytokine secretion assay in response to SIK2 inhibitors

Primary BMDMs were obtained from C57BL/6J mice which were maintained under standard specific pathogen-free conditions. BMDMs were differentiated for six days in DMEM (Gibco) containing 10% FCS, Penicillin/Streptomycin (Gibco), 0.1 mM 2-Mercaptoethanol (Gibco) and L929-conditioned medium. On day 6, BMDMs were seeded in 96-well plates at $2.5x10^4$ cells per well in 50 μL culture medium (differentiation medium without L929 supernatants), followed by incubation at 37°C for 4 h. Cells were incubated with compounds (25 μL of a 4X stock per well) for 2 h followed by stimulation with LPS (ultrapure LPS-EB from Invivogen, 100 ng/mL final concentration) dispersed in culture medium (25 μL per well) for 18 h. After LPS stimulation, the cell culture medium was removed and clarified by centrifugation for 5 min at 400 × g. Concentrations of TNFα or IL-10 in the supernatants were determined using mouse TNFα ELISA ready-set-go (eBioscience) according to the manufacturer's instructions. BMDMs were detached with 5 mM EDTA in PBS, transferred to a white plate and viability was assessed using the CellTiter-Glo luminescent cell viability assay (Promega) following to the manufacturer's instructions. Experiments were performed in biological duplicates and technical triplicates.

CRCT3 phosphorylation site monitoring by PRM after SIK2 inhibitor treatment

Murine BMDMs were treated with HG-9-91-01 (300 nM), AZD-7762 (300 nM), PF-03814735 (300 nM), UCN-01 (100 nM), dasatinib (300 nM), AT-9283 (1000 nM) for 30 min at 37°C, followed by stimulation with LPS (ultra-pure LPS-EB from Invivogen, 100 ng/mL final concentration) for 30 min at 37°C. Each treatment was performed on a single 10 cm dish (about 90% confluence, $0.5\text{-}1x10^7$ cells, 0.1% final DMSO concentration). After treatment, cells were washed twice with phosphate-buffered saline and lysed by scraping in the presence of 200 μL lysis buffer (40 mM Tris-HCl pH 7.6, 8 M urea, protease inhibitors (SigmaFast, Sigma) and phosphatase inhibitor cocktail at 1× final concentration). Disulfide bonds were reduced (10 mM DTT, 45 min, 37°C) and alkylated (55 mM chloroacetamide, 30 min, room temperature, darkness). A total of 500 μg protein extract was diluted with digestion buffer (50 mM Tris-HCl pH 7.6) to reduce the urea concentration to <1.6 M, and subsequently digested with trypsin (1:100 protease:protein ratio). After a predigestion step (4 hours, 37°C), another aliquot of trypsin was added (1:100 protease:protein ratio), and the sample was further incubated overnight at 37°C. The tryptic digest was acidified with formic acid (final concentration 1% v/v), desalted using C18 Sep-Pak columns according to the manufacturer's instructions (Waters), and dried down in a vacuum centrifuge. Phosphopeptides were enriched from digests using Fe-IMAC as previously described (*59*). Fe-IMAC eluate was desalted using C18 StageTips as described (*60*), and dried down in a vacuum centrifuge.

To monitor the phosphorylation of the three CRTC3 phosphorylation sites, a parallel reaction monitoring assay (PRM) was set up. SIK2-dependent phosphorylation on CRTC3 was reported for Ser62, Ser162, Ser329, Ser370 (*28*). A spectral library for the surrogate peptides LTQYHGGpSLPNVSQLR (CRCT3_Ser62) and LFSLpSNPSLSTTNLSGPSR (CRCT3_Ser370) was constructed using the Skyline 3.7.0 software (*61*) and a MaxQuant derived msms.txt file. Precursor charge states and transitions were automatically chosen from the spectral library and the transitions manually refined to include site determining ions for each phospho site. In addition, the PRTC retention time calibration mixture (Pierce) was monitored. A scheduled inclusion list with 10 min monitoring windows was exported for the LC-MS method (table S8).

Nanoflow LC-ESI-MS/MS measurements were performed with a Dionex Ultimate 3000 UHPLC+ system coupled to a Fusion Lumos Tribrid mass spectrometer (Thermo Fisher Scientific). After reconstitution in 50 mM citric acid, 0.1% FA containing 25 fmol/μL PRTC retention time calibration mixture (Pierce), 1/4th of each Fe-IMAC enrichment was injected. Peptides were delivered to a trap column (75 μm × 2 cm, packed in-house with 5 μm C18 resin; Reprosil PUR AQ, Dr. Maisch) and washed using 0.1% formic acid at a flow rate of 5 μL/min for 10 min. Subsequently, peptides were transferred to an analytical column (75 μm × 45 cm, packed in-house with 3 μm C18 resin; Reprosil Gold, Dr. Maisch) applying a flow rate of 300 nL/min and separated using a 50 min linear gradient from 4% to 35% LC solvent B (0.1% FA, 5% DMSO in ACN) in LC solvent A (0.1% FA in 5% DMSO). The mass spectrometer was operated in positive ionization mode. The acquisition method contained two separate experiments. The acquisition was set up to switch between experiments after one duty-cycle. The first experiment consisted of a full scan MS1 spectrum recorded in the Orbitrap mass analyzer from 360 to 1300 m/z at a resolution of 15,000 (at m/z 200) using an AGC target value of 4e5 and a maximum injection time of 10 ms. The second experiment consisted of a tMS2 PRM scan triggering MS2 scans based on a scheduled list containing m/z and charge information. For the tMS2 PRM scan, the scheduled precursors were isolated (isolation window 0.4 m/z) and fragmented via HCD using

Downloaded from http://science.sciencemag.org/ on November 30, 2017

a normalized collision energy of 28%. MS2 spectra were recorded in the Orbitrap mass analyzer from 100 to 2000 m/z at a resolution of 15,000 using an AGC target value of 2e5 and a maximum injection time of 250 ms.

The generated RAW files were imported into Skyline for data filtering and analysis. The transitions were extracted with Phospho (S, T, Y) as structural modification, allowing precursor charges 2, 3 and ion types b, y. The library ion match tolerance was set to 0.05 m/z and transitions were extracted using the centroided product mass analyzer with 20 ppm mass accuracy with high-selectivity extraction switched on (including all matching scans). Peaks were integrated using the automatic peak finding function followed by the manual curation of all peak boundaries and transitions (table S8). The summed area under the fragment ion traces data for every transition was exported for data visualization in Microsoft Excel and GraphPad Prism 5. Intensity values of the samples were normalized to the total intensity of all eluting features extracted from MaxQuant's allpeptides.txt to correct for unequal loading. Corrected data was normalized to the intensity of the DMSO control to display changes in CRTC3 phosphorylation introduced by SIK2 inhibition.

Implementation of elastic net for drug target deconvolution

The predicted percentage of inhibition values (using the 4 parameter model fits) for each target:drug combination at 100 and 300 nM were used as predictors for the elastic net model. In order to evaluate the stability of selection of a target, we employed a bootstrap approach as previously described (*62*). In short, for each dose, we randomly drew (with replacement) 100 pairs of kinase inhibitor target profiles and TNFα production measurement and fed the randomly drawn samples into the elastic net model. The results are summarized by two statistic – selection frequency, showing how many times a target is selected in the 100 bootstrap samples; and effect size, the coefficient multiplied by the standard deviation of the K_d^{app}s of a target. The effect size reflects how much the TNFα production changes under a unit change of a specific target. The models were fitted using the CRAN package glmnet (version 2.0-10). The alpha and regularization parameter lambda were optimized using a five-fold cross-validation. Most features were stably selected at a wide range of alpha, leading to a final selection of alpha = 0.1 to have a good compromise between model accuracy and sparsity. Using this alpha, lambda was chosen such that the prediction error in the validation set was minimal.

Dose-dependent cell viability and time-resolved cell proliferation assays for combination treatments and TPM3-NTRK1 fusion inhibition

Cell viability was determined using the alamarBlue cell viability assay (Thermo Fisher Scientific) in 96-well plates. For A-431 (epidermoid cancer) and PC-9 (lung cancer) cells (cultivated in RPMI-1640 with 10% FBS, Biochrom), ACHN (renal cancer) and IGROV-1 (ovarian cancer) cells (IMDM, 10% FBS, Biochrom), 2,000 cells were seeded per well. For KM12 cell viability, 1,000 cells were seeded per well in IMDM medium with 10% FBS (Biochrom). On the following day, the cells were exposed to different concentrations of a specified inhibitor ranging from 1 nM to 10 μM. The cells were incubated for 72 h at 37°C and 5% CO_2. Cell viability assays were performed by adding 10% alamarBlue reagent to each well. The reduction from resazurin to resorufin was measured after 4 h using a fluorescence spectrophotometer (BMG Labtech) at 544 nm (excitation) and 584 nm (emission). This assay does not distinguish between viability and proliferation. For simplicity, we refer to viability, acknowledging that this may also mean proliferation.

Time-resolved cell proliferation assays were performed for A-431, PC-9, ACHN and IGROV-1 cells in 96-well plates containing 2,000 cells per well. Cells were exposed to gefitinib (LC Laboratories) and AZD-4547 (Selleckchem) for 0, 12, 24, 48 and 72 h. The selected drug concentration for each cell line was based on the cellular EC_{50} of the drug used (A-431: gefitinib 1 μM, AZD-4547 5 μM; PC-9: gefitinib 100 nM, AZD-4547 5 μM; IGROV-1: gefitinib 100 nM, AZD-4547 5 μM; ACHN: gefitinib 1 μM, AZD-4547 1 μM). The number of viable cells was measured with the CellTiter-Glo (Promega) reagent. Celltiter-Glo reagent (100 μL) was added to each well, the plate was briefly shaken at 700 r.p.m. and incubated in a microplate reader at 37°C for 8 min. Measurement of luminescence was performed after 10 min in a fluorescence spectrophotometer (FluoStar Omega, BMG Labtech). Data from the cellular assays were analyzed using GraphPadPrism (version 5.03).

siRNA and drug treatment for SRC and BMP receptor signaling

NCI/ADR-RES cells were seeded in 200 μL IMDM medium (Biochrom GmbH, supplemented with 10% FBS and 1% antibiotics) at a density of 1×10^4 cells/mL, U-2 OS cells were seeded in 200 μL DMEM medium (Biochrom GmbH, supplemented with 10% FBS and 1% antibiotics) at a density of 5×10^3 cells/mL. The cells were incubated overnight at 37°C and 5% CO_2. Lyophilized siRNA (for SRC, BMPR1A, ACVR1, ACVR1B, Qiagen) was reconstituted by the addition of sterile RNAse-free water according to the instructions provided by the manufacturer. The siRNA was further diluted in Opti-MEM (GIBCO) before addition of the transfection reagent INTERFERin (PolyPlus, peqlab). The mixture was vortexed for 10 s and incubated for 10 min at room temperature. Medium was removed from the cells and fresh medium was added. The transfection mixture was homogenized by swirling and added to the well. The cells were incubated for 144 h and cell viability was assessed by an alamarBlue assay according to the manufacturer's instruction (Thermo Fisher Scientific) as described above.

For saracatinib treatment of U-2 OS and NCI/ADR-RES control cells, cells were seeded in a 96-well plate in a density of 1000 and 2000 cells per well, respectively. Drug was added in increasing concentrations (3 nM, 10 nM, 30 nM, 100 nM, 300 nM, 1 μM, 3 μM, 30 μM in DMSO) and incubated for 72 h at 37°C and 5% CO_2. Cell viability was assessed by an alamarBlue assay according to the manufacturer's instruction (Thermo Fisher Scientific) as described above.

For Western Blot analysis, $3x10^6$ U-2 OS cells were seeded in a 10 cm cell culture dish and treated with inhibitors (dasatinib 1 μM, gilteritinib 1 μM, saracatinib 1 μM, 100 nM, 10 nM in DMSO) for 30 min prior to addition of 100 ng/ml BMP2 (#4697, Cell signaling technology), followed by 45 min incubation before cells were lysed using an NP40-based lysis buffer as described earlier. Western blotting was performed using the following antibodies: pSMAD1/5 (Ser463/465)/SMAD9 (465/467) (D5B10, Cell Signaling Technology), pSRC (Y416, D49G4, Cell Signaling Technology), c-SRC (sc-18, Santa Cruz Biotechnology) and β-actin (sc-47778, Santa Cruz Biotechnology).

Cloning, expression, purification, crystallization, and structure determination of NQO2

The codon-optimized full-length DNA sequence encoding for the human NQO2 enzyme (ThermoFisher Scientific) with a C-terminal His_6-affinity tag was cloned into the expression plasmid pET28. For protein expression, the plasmid was transformed in *E. coli* BL21 (DE3) (Novagen). The cells were grown in 2YT medium supplemented with 50 μg/mL kanamycin at 37°C until an optical density of 1 was reached. Protein expression was induced by adding 1 mM isopropyl-β-D-thiogalactoside (IPTG) and continued at 30°C overnight. Cells were harvested by centrifugation, resuspended in 50 mM Tris-HCl pH 7.4, 300 mM NaCl, 10 mM imidazole (lysis buffer) supplemented with complete protease inhibitor cocktail (Roche) and lysed by sonication. Protein purification was performed by Ni-affinity chromatography (Ni-NTA superflow, Qiagen). The protein buffer was exchanged to 50 mM Tris-HCl pH 8, and the protein concentration was adjusted to 50 mg/mL using centrifugal filter devices (Amicon Ultra Centrifugal Filter Device, Millipore), aliquoted and stored at -80°C until required. For co-crystallization, NQO2 in 50 mM Tris-HCl pH 8, 10 μM flavin adenine dinucleotide and 1 mM dithiothreitol was mixed with pacritinib, crenolanib or volitinib (4 mM stock solution in dimethyl sulfoxide) to a final concentration of 7.5 mg/mL NQO2 and 100 μM of the inhibitor prior to crystallization. Crystals were grown in 180 mM triammonium citrate, 2.2 M ammonium sulphate (crenolanib) and 200 mM sodium sulphate, 2.2 M ammonium sulphate (pacritinib, volitinib) at 20°C. Data was collected at the PXI beam line of the Swiss Light Source (SLS, Villigen Switzerland). Diffraction data were processed with XDS (*63*, *64*) to 1.35 Å (crenolanib, pacritinib) and 1.9 Å (volitinib) resolution and crystals belonged to the space group $P2_12_12_1$. The resolution thresholds were chosen using the correlation coefficient of random half-data sets (1/2 CC) of about 50% (*65*–*67*). For all data sets the same set of FreeR reflections was used. The structures

Downloaded from http://science.sciencemag.org/ on November 30, 2017

were solved by placing the coordinates of human NQO2 (PDB code 2BZS) in the asymmetric crystal unit using rigid-body refinement, followed by restrained refinement in REFMAC5 (68–70). Well-defined peaks for pacritinib, crenolanib and volitinib were visible in the corresponding difference density maps. Iterative cycles of manual building and refinement were performed in COOT (68, 71) and REFMAC5. Structural superpositions were achieved with SSM (72) and interactions analyzed by LIGPLOT (73). All structural figures were prepared with PyMol (Delano Scientific). Full data collection and refinement statistics are reported in the supplementary text.

Crystallization and structure determination of MELK

Protein production was performed as previously described (74). Crystallization experiments were established using the dephosphorylated MELK protein (residues 2-340) plus 1 mM DTT and 0.5 mM inhibitor dissolved in DMSO. Crystals were grown in hanging drops prepared by mixing equal volumes (1-2 μL) of protein solution at a concentration of 7 mg/mL and reservoir solution containing 10-20% PEG 3350 or PEG 4000, 600 mM NaCl and 100 mM Bis-Tris pH 6.5. After setting the drops, 1 μL 14.3 M β-mercaptoethanol was added to the 500 μL reservoir. Streak seeding was essential in order to obtain diffraction quality crystals. Two different crystal morphologies were observed. MELK complexed with nintedanib, PF-3758309, K-252a and defactinib yielded rectangular, prism-shaped crystals as described (74); whilst the MELK-BI-847325 complex produced cubic crystals. Crystals were transferred in a cryoprotectant solution (15% PEG 3350, 600 mM NaCl and 100 mM Bis-Tris pH 6.5 and 30% glycerol) prior to flash-cooling in liquid nitrogen. X-ray diffraction data were collected at the European Synchrotron Radiation Facility (ESRF) in Grenoble (beam line ID23-1). Crystals of MELK complexed with nintedanib, PF-3758309, K-252a and defactinib were of space group $P2_12_12_1$; whilst crystals of MELK complexed with BI-847325 belonged to space group $I4_132$. Using an internal MELK structure as a search model, data were processed with iMOSFLM (68, 75) or XDS (63, 64) merged with SCALA (68, 76) and phased via molecular replacement with Phaser (68, 77). Refinement of the structures was achieved using REFMAC (68–70) and COOT (68, 71). Full data collection and refinement statistics are reported in the supplementary text.

Drug-perturbed phosphoproteome analysis

The ERBB2 overexpressing breast cancer cell line BT-474 was grown in DMEM/Ham's F-12 medium (Biochrom) supplemented with 15% (v/v) FBS (Biochrom) and 1% (v/v) antibiotic/antimycotic solution (Sigma). BT-474 cells were treated with 1 μM of each compound for 30 min in four biological replicates. After treatment, cells were washed twice with PBS (Sigma Aldrich) and lysed by scraping in the presence of 400 μL lysis buffer (40 mM Tris-HCl pH 7.6, 8 M urea, EDTA-free protease inhibitor complete mini (Roche) and phosphatase inhibitor cocktail at 1× final concentration). Lysate was transferred into a 1 mL reaction vessel and centrifuged for 1 h at 21,000×*g*. A total of 2 mg protein per experimental condition was digested. Disulfide bonds were reduced with DTT at a final concentration of 10 mM for 45 min at 37°C. Cysteine residues were alkylated with 55 mM chloroacetamide for 30 min at room temperature in the dark. The sample was diluted with three volumes of 40 mM Tris-HCl pH 7.6 to decrease the urea concentration to 1.5 M. Trypsin was added to a protease-to-protein ratio of 1:50 (w/w) and digestion was performed overnight at 37°C and 700 rpm on a thermoshaker. The following day, the samples were cooled to room temperature and acidified with 0.5% TFA. Following the precipitation of insoluble debris at 5,000×*g*, the supernatant was desalted using 50 mg Sep-Pak columns (Waters) and a vacuum manifold. Columns were primed with 1 mL solvent B (0.07% TFA, 50% ACN) and equilibrated with 2 mL solvent A (0.07% TFA in deionized water). The sample was then slowly passed through the column to allow proper peptide binding. Peptides were washed three times with 1 mL solvent A and then eluted into a reaction vessel using 2×150 μL solvent B. Finally, the samples were frozen at -80°C and lyophilised in a vacuum concentrator. Phosphopeptides were enriched from digests using Fe-IMAC as previously described (59). Dried phosphopeptides were labeled using TMT 6-plex at a final concentration of 6.67 mM according to instructions provided by the manufacturer. One TMT channel was used for each drug treatment (126=control, 127=lapatinib, 128=afatinib, 129=canertinib, 130=dacomitinib, 131=sapitinib). Subsequently, peptides were separated into six fractions using high pH reversed-phase stage tips (five discs, Ø 1.5 mm, C18 material, 3M Empore per micro-column were used). Stage tips were primed with 40 μL 50% ACN, 25 mM NH_4COOH (pH 10) and equilibrated with 2×40 μL 25 mM NH_4COOH (pH 10). The sample was then slowly passed through the column and the flow-through collected and applied to a low pH micro-column for desalting as previously described (78). Peptides were fractionated with increasing ACN concentrations (5%, 7.5%, 10%, 12.5%, 15%, 17.5% and 50% ACN) in 25 mM NH_4COOH, pH 10. The desalted flow-through was combined with the 17.5% fraction and the 50% fraction with the 5% fraction to give a total of six fractions. All samples were lyophilised. LC-MS/MS analysis of TMT 6-plex-labeled phosphopeptides was performed using a Dionex Ultimate3000 nano HPLC coupled to an Orbitrap Fusion (Thermo Scientific) mass spectrometer. Peptides were dissolved in 15 μL 0.5% formic acid and one third was injected, Duplicate analyses were performed for each stage tip fraction. Peptides were desalted on a trap column (Acclaim C18 PepMap100, 75 μM i.d. × 2 cm) in 0.1% FA and separated on an analytical column (Acclaim C18 PepMap RSLC, 75 μM i.d. ×15 cm) using a 120 min gradient from 3-25% B (0.1% FA, 5% DMSO in 100% ACN) in solution A (0.1% FA, 5% DMSO in water). Full scan MS1 spectra were acquired over a range of 300-1700 *m/z* and at a resolution of 60,000 (at *m/z* 200) in the Orbitrap (AGC target value 4e5, maximal injection time 50 ms). Fragmentation was performed using CID at 40% NCE (AGC target value 4e4, maximal injection time 60 ms) in the ion trap. MS2 ions were recorded in the linear ion trap. For MS3 spectral acquisition, fragment ions were selected by multi-notch isolation, allowing a maximum of 10 notches and an ion trap isolation width of 2 Da. These ions were fragmented by HCD at 55% NCE (AGC target value 1e5, maximal injection time 120 ms). The resultant MS3-fragment ions were recorded in the Orbitrap over an *m/z* range of 100-500 and a resolution of 60,000 (at *m/z* 200). Proteins and peptides were identified and quantified using MaxQuant (v 1.5.3.8) with enabled MS3-based TMT quantification using default parameters and the UniprotKB database (human, 42,145 entries, downloaded 01.02.2016). Phosphorylation on S, T and Y and oxidation of M was specified as variable modification. Within one replicate, the sum of phosphopeptide intensities per TMT channel were normalized to the sum of intensities of its DMSO control (TMT 126). Subsequently, the average intensities for each phosphopeptide per replicate was normalized to the average intensity of the same phosphopeptide across all replicates. The latter corrects for batch effects introduced by the MS2 quantification and allows for direct intensity comparison across replicates. Data was further analyzed by Perseus (v 1.5.0.15) (79). Fold changes for each inhibitor against the vehicle control were calculated per peptide and tested for significance using a t-test and threshold p-value < 0.01. Only phosphorylation sites that were significantly-regulated (P value < 0.01) in at least three from four biological replicates and at least four from five inhibitors were considered as core pathway members. Protein-protein interactions were extracted using the String database (v 10) (80) (combined score > 0.4) and visualized in Cytoscape (v 3.1.0). ERBB pathway annotation was performed based on the Reactome plug-in (FDR < 0.01) in Cytoscape and only annotations including the terms ERBB, ERBB2, AKT, PIK3, MEK, MAPK1/3 and MTOR were selected.

Selected phosphosites were confirmed by Western Blot analysis using antibodies against pERBB2 Y1248 (#2247, Cell Signaling Technology), pCHEK1 S280 (orb129560, Biorbyt), pAKT S473 (#4060, Cell Signaling Technology) and β-actin C4 (sc-47778, Santa Cruz Biotechnology) in a separate biological replicate.

Kinobead expression profiling of 15 NSCLC cases

Fresh primary lung tumor tissues and surgical margin (nearby healthy) tissue samples were collected from consenting patients of Tartu University Hospital and the clinical and histopathological information was obtained from pathology reports. For protein extraction, the defrosted tissue was quickly dissected using surgical scissors, washed with pre-cooled PBS to remove residual blood and homogenized using a dounce homogenizer with compound pulldown lysis buffer (0.8% NP40, 50 mM Tris-HCl pH 7.5, 5% Glycerol,

Downloaded from http://science.sciencemag.org/ on November 30, 2017

1.5 mM $MgCl_2$, 150 mM NaCl, 1 mM Na_3VO_4, 25 mM NaF, 1 mM DTT) and freshly added protease (2x protease inhibitor mixture; Roche Applied Science) and phosphatase inhibitors. The homogenate was incubated on ice for 30 min and then centrifuged at 2°C for 30 min at 20,000 x g to remove cell debris. Supernatants were collected, aliquoted, frozen in liquid nitrogen, and stored at -80°C until further use. Protein concentration in lysates was determined by the Bradford assay.

Kinobead pulldowns were performed in two replicates as described (*81*). Briefly, 5 mg of tissue lysate were incubated with 100 µL of kinobeads-α at 4°C for 4 h. After washing of the beads, bound proteins were eluted with 2x NuPAGE-LDS sample buffer (Invitrogen), and subsequently reduced and alkylated by 10 mM DTT and 55 mM iodoacetamide. The samples were concentrated on a SDS gel and in-gel trypsin digestion was performed. Peptides of kinobeads enriched NSCLC samples were dissolved in 0.1% formic acid and subjected to analysis on an Eksigent nanoLC-Ultra1D+ (Eksigent) coupled to a LTQ Orbitrap Velos (Thermo Scientific) for LC-MS/MS analysis. Peptides were delivered to a trap column (100 µm inner diameter x 2 cm, packed with 5 µm C18 resin, Reprosil PUR AQ; Dr. Maisch) at a flow rate of 5 µL/min in 100% buffer A (0.1% FA in HPLC grade water). Subsequently, peptides were transferred to an analytical column (75 µm x 40 cm C18 column Reprosil PUR AQ, 3 µm; Dr. Maisch) and separated using a 210 min gradient from 2% to 35% of buffer B (0.1% FA in acetonitrile) at 300 nL/min flow rate. The Orbitrap was operated in data-dependent mode, automatically switching between MS and MS2. Full scan MS spectra were acquired in the Orbitrap at 60,000 resolution. Internal calibration was performed using the ion signal $(Si(CH_3)_2O)_6$ H+ at m/z 445.120025 present in ambient laboratory air. Tandem mass spectra were generated for up to eight peptide precursors in the linear ion trap for fragmentation by using collision-induced dissociation (CID).

Progenesis (version 3.1; Nonlinear Dynamics) was used for intensity-based label-free quantification. Briefly, after selecting one sample as a reference, the retention times of all eluting precursor m/z values in all other samples within the experiment were aligned creating a list of "features" representing the same peptide in each sample. Features with two to six charges were included for further analysis. Features with two or less isotopes were excluded. After alignment and feature filtering, replicate samples were grouped together, and raw abundances of all features were normalized to determine a global scaling factor for correcting experimental variation such as differences in the quantity of protein loaded into the instrument. Given that multiple MS/MS spectra are frequently collected for the same feature (precursor ion) across all the samples, the precursor intensities were ranked, and the MS/MS spectra of the five most intense precursors for each feature were transformed into peak lists and exported to generate Mascot generic files. The Mascot generic files were searched against the protein sequence database IPI human (v. 3.68, 87,061 sequences) using Mascot (v.2.2, Matrix Science). Search parameters were as follows: fixed modification of carbamidomethylation of cysteine residues, variable modification of serine, threonine, and tyrosine phosphorylation and methionine oxidation, trypsin as proteolytic enzyme with up to two missed cleavages, precursor ion mass tolerance of 5 ppm, fragment ion mass tolerance of 0.6 Da, decoy search enabled. Search results for spectrum to peptide matches were exported in.xml format and then imported into Progenesis to enable the combination of peptide quantification and identification. Peptides with mascot ion scores >33 ($P < 0.05$ identity threshold) were retained, and only unique peptides for corresponding proteins were used for identification and quantification. Single peptide identifications were removed except for identified kinases. For protein quantification, the feature intensities of all unique peptides of a protein were summed up.

To identify differentially expressed kinases between normal and tumor samples, a paired t-test on the log transformed MS intensity (median centered, quantified by Progenesis) was performed. The false discovery rates (FDR) for kinases were calculated from the resulting P values using Benjamini-Hochberg correction.

Immunohistochemistry staining of NSCLC patient tissue

Immunohistochemical staining and analysis of human patient material was performed on tissue microarrays (TMA) as previously described (*82*). All tissues analyzed in this study were obtained from patients at the Institute of Surgical Pathology, University Medical Center Freiburg, Germany. This study was approved by the Ethics Committee of the University Medical Center Freiburg (no. EK 10/12). The patient cohort (n=375) comprised adenocarcinomas (n=186) and squamous cell carcinomas (n=189). Where required, histological diagnoses were verified according to current WHO classification with immunohistochemistry (*83*). The maximum follow-up time was 210 months. Clinical data comprising pTMN, resection status (R), gender and patient age at diagnosis are summarized in table S15. Immunohistochemical staining was performed on a Discovery XT automated stainer (Ventana) using the following primary antibodies: MELK (1:50, Sigma-Aldrich), DDR1 (1:50, Biozol), and EGFR (pharmDx™-kit, DAKO). Signal detection was performed using peroxidase-DAB (diaminobenzidine)-MAP kit (Roche, Ventana). The immunohistological expression of the membrane-binding EGFR, the nuclear MELK and the cytoplasmatic DDR1 were classified into four levels according to specific staining intensity: Score 0, 1+, 2+, 3+.

Cell lines, inhibitors, cytokines and antibodies for cabozantinib repurposing

Low-passage murine Ba/F3, WEHI-3B and leukemia cell lines THP-1, OCI-AML3, OCI-AML5, U-937, KG-1a, NB-4, HL-60, SD-1, K-562, MV-4-11, MOLM-13, MONO-MAC-1, MONO-MAC-6, EOL-1 KASUMI-1 were obtained from the German Collection of Microorganisms and Cell Cultures (DSMZ) and cultured as previously described and according to instructions provided by the manufacturer (*84*). Stable Ba/F3 cells were generated as previously described (*84*–*86*). The kinase inhibitors quizartinib, crenolanib, cabozantinib were purchased from Selleckchem. Golvatinib was purchased from MedChemExpress. Recombinant human FLT3 ligand (FL) was obtained from Promokine, recombinant murine interleukin (IL)-3 and recombinant human stem cell factor (SCF) were obtained from Immunotools. The following antibodies were used: STAT5 (sc-835), FLT3 (sc-480) (both Santa Cruz Biotechnology); α-tubulin (T6199, Sigma-Aldrich); pSTAT5 (MA5-14973, Thermo Fisher Scientific), pFLT3 (#3463, Cell Signaling Technology). Immunoblot analysis was performed as previously described (*84*).

Proliferation and MTS assay for cabozantinib repurposing

For proliferation assays, 3×10^5 cells/mL and 4×10^4 cells/mL of leukemia and Ba/F3 cell lines, respectively, were seeded in growth medium in the presence or absence of inhibitors and cytokines. Viable cells were counted after 72 h by trypan blue exclusion using the cell viability analyzer Vi-Cell XR (Beckman Coulter). Determination of the 50% inhibitory concentration (IC_{50}) of the inhibitors was calculated using GraphPad Prism (v.5.03). For MTS assays, 7.5×10^3 – 40×10^3 cells/100 µL (cell line dependent) were seeded and incubated in the presence or absence of inhibitors for 72 h and subjected to a Cell Titer 96 Aqueous One solution cell proliferation assay according to the instructions provided by the manufacturer (Promega).

Immunofluorescence staining

U-2 OS cells were grown on cover slips and transiently transfected with pcDNA6.2-V5-HisA-FLT3 wild-type and mutant constructs using PoliFect (Qiagen) according to the guidelines supplied by the manufacturer. 48 h post-transfection, cells were treated for 6 h in the presence or absence of 50 nM cabozantinib. Glycoconjugates in the membrane were stained thereafter using anti-wheat germ agglutinin (WGA) 488 fluorescein conjugate (1:1,000, W11261, Invitrogen) at 37°C for 10 min. After washing with PBS, cells were fixed with PBS, 2% formaldehyde (37% stock solution; Merck Schuchardt) for 10 min, permeabilized with PBS, 0.5% Triton X-100 (Carl Roth) for 10 min and blocked for 1 h with PBS, 2% BSA (Albumin Fraction V, AppliChem). Cells were then incubated with polyclonal rabbit anti-FLT3 antibody (1:200, sc-480, SantaCruz Biotechnology) for 1 h. After extensive washing with PBS, 0.1% Tween 20 (Carl Roth), secondary antibody incubation was performed for 1 h with anti-rabbit IgG (H+L), F(ab')2 fragment Alexa Fluor 594 Conjugate (1:500, 8889, Cell Signaling). Counterstaining with 1 µg/mL 4',6-diamidino-2-phenylindole (DAPI; Sigma Aldrich) was then performed for 10 min. For mounting fluorescence, mounting medium (Dako) was used. Specimens were analyzed utilizing a confocal fluorescence

Downloaded from http://science.sciencemag.org/ on November 30, 2017

laser scanning system (TCS SP5 II; Leica). For image acquisition and processing, the LAS AF Lite Software (Leica) was used.

AML xenograft model

NOD.Cg-Prkdc^{scid} IL2rg^{tm1Wjl}/SzJ mice (NSG; The Jackson Laboratory) were maintained under specific pathogen-free conditions in the research animal facility of the Helmholtz Center Munich, Germany. Animals accessed food and water *ad libitum*, and were housed with a 12 h light–dark cycle and constant temperature. All animal trials were performed in accordance with the current ethical standards of the official committee on animal experimentation (written approval by Regierung von Oberbayern, number 55.2-1-54-2532-95-10). AML cell lines MOLM13 and OCI-AML3 were lentivirally-transduced to express a recombinant codon-optimized form of firefly luciferase (effluc) (*87*). Production of lentiviral particles, lentiviral transduction and *in vivo* bioluminescence imaging (BLI) were performed as previously described (*88*). Cells transgenic for effluc were injected into the tail vein of mice. To visualize effluc-expressing cells, D-Luciferin (BIOMOL GmbH) was injected at 150 mg/kg into the tail vein of mice. The Living Image software 4.4 (Caliper Life Sciences) was used for data acquisition and quantification of light emission using a scale with a minimum of 2×10^3 photons per second per cm^2 per solid angle of one steradian (sr). When the bioluminescence imaging (BLI) signal reached about 1×10^8 photons/(s cm^2 sr), mice were treated with cabozantinib (60 mg/kg) or solvent (30% 1,2-Propandiol, 5% Tween80, 65% D5W) by oral gavaging over one or two weeks, four doses per week. No randomization or blinding was done. After the end of the treatment, tumor load was again determined by BLI.

REFERENCES AND NOTES

1. P. Wu, T. E. Nielsen, M. H. Clausen, FDA-approved small-molecule kinase inhibitors. *Trends Pharmacol. Sci.* **36**, 422–439 (2015). doi: 10.1016/j.tips.2015.04.005; pmid: 25975227
2. D. Fabbro, S. W. Cowan-Jacob, H. Moebitz, Ten things you should know about protein kinases: IUPHAR review 14. *Br. J. Pharmacol.* **172**, 2675–2700 (2015). doi: 10.1111/bph.13096; pmid: 25630872
3. M. W. Karaman *et al*., A quantitative analysis of kinase inhibitor selectivity. *Nat. Biotechnol.* **26**, 127–132 (2008). doi: 10.1038/nbt1358; pmid: 18183025
4. Y. Gao *et al*., A broad activity screen in support of a chemogenomic map for kinase signalling research and drug discovery. *Biochem. J.* **451**, 313–328 (2013). doi: 10.1042/BJ20121418; pmid: 23398362
5. M. I. Davis *et al*., Comprehensive analysis of kinase inhibitor selectivity. *Nat. Biotechnol.* **29**, 1046–1051 (2011). doi: 10.1038/nbt.1990; pmid: 22037378
6. T. Anastassiadis, S. W. Deacon, K. Devarajan, H. Ma, J. R. Peterson, Comprehensive assay of kinase catalytic activity reveals features of kinase inhibitor selectivity. *Nat. Biotechnol.* **29**, 1039–1045 (2011). doi: 10.1038/nbt.2017; pmid: 22037377
7. J. Bain *et al*., The selectivity of protein kinase inhibitors: A further update. *Biochem. J.* **408**, 297–315 (2007). doi: 10.1042/BJ20070797; pmid: 17850214
8. M. A. Fabian *et al*., A small molecule–kinase interaction map for clinical kinase inhibitors. *Nat. Biotechnol.* **23**, 329–336 (2005). doi: 10.1038/nbt1068; pmid: 15711537
9. S. P. Davies, H. Reddy, M. Caivano, P. Cohen, Specificity and mechanism of action of some commonly used protein kinase inhibitors. *Biochem. J.* **351**, 95–105 (2000). doi: 10.1042/bj3510095; pmid: 10998351
10. J. M. Elkins *et al*., Comprehensive characterization of the Published Kinase Inhibitor Set. *Nat. Biotechnol.* **34**, 95–103 (2016). doi: 10.1038/nbt.3374; pmid: 26501955
11. J. T. Metz *et al*., Navigating the kinome. *Nat. Chem. Biol.* **7**, 200–202 (2011). doi: 10.1038/nchembio.530; pmid: 21336281
12. HMS LINCS Database, http://lincs.hms.harvard.edu/db/ (2016).
13. M. Bantscheff *et al*., Quantitative chemical proteomics reveals mechanisms of action of clinical ABL kinase inhibitors. *Nat. Biotechnol.* **25**, 1035–1044 (2007). doi: 10.1038/nbt1328; pmid: 17721511
14. G. Médard *et al*., Optimized chemical proteomics assay for kinase inhibitor profiling. *J. Proteome Res.* **14**, 1574–1586 (2015). doi: 10.1021/pr5012608; pmid: 25660469
15. M. Wilhelm *et al*., Mass-spectrometry-based draft of the human proteome. *Nature* **509**, 582–587 (2014). doi: 10.1038/nature13319; pmid: 24870543
16. M. P. Patricelli *et al*., In situ kinase profiling reveals functionally relevant properties of native kinases. *Chem. Biol.* **18**, 699–710 (2011). doi: 10.1016/j.chembiol.2011.04.011; pmid: 21700206
17. J. J. Sutherland, C. Gao, S. Cahya, M. Vieth, What general conclusions can we draw from kinase profiling data sets? *Biochim. Biophys. Acta* **1834**, 1425–1433 (2013). doi: 10.1016/j.bbapap.2012.12.023; pmid: 23333421
18. A. F. Rudolf, T. Skovgaard, S. Knapp, L. J. Jensen, J. Berthelsen, A comparison of protein kinases inhibitor screening methods using both enzymatic activity and binding affinity determination. *PLOS ONE* **9**, e98800 (2014). doi: 10.1371/journal.pone.0098800; pmid: 24915177
19. P. P. Graczyk, Gini coefficient: A new way to express selectivity of kinase inhibitors against a family of kinases. *J. Med. Chem.* **50**, 5773–5779 (2007). doi: 10.1021/jm070562u; pmid: 17948979
20. J. C. M. Uitdehaag, G. J. R. Zaman, A theoretical entropy score as a single value to express inhibitor selectivity. *BMC Bioinformatics* **12**, 94 (2011). doi: 10.1186/1471-2105-12-94; pmid: 21486481
21. A. C. Cheng, J. Eksterowicz, S. Geuns-Meyer, Y. Sun, Analysis of kinase inhibitor selectivity using a thermodynamics-based partition index. *J. Med. Chem.* **53**, 4502–4510 (2010). doi: 10.1021/jm100301x; pmid: 20459125
22. S. Knapp *et al*., A public-private partnership to unlock the untargeted kinome. *Nat. Chem. Biol.* **9**, 3–6 (2013). doi: 10.1038/nchembio.1113; pmid: 23238671
23. A. J. Kooistra *et al*., KLIFS: A structural kinase-ligand interaction database. *Nucleic Acids Res.* **44**, D365–D371 (2016). doi: 10.1093/nar/gkv1082; pmid: 26496949
24. Z. Zhao *et al*., Exploration of type II binding mode: A privileged approach for kinase inhibitor focused drug discovery? *ACS Chem. Biol.* **9**, 1230–1241 (2014). doi: 10.1021/cb500129t; pmid: 24730530
25. J. F. Ohren *et al*., Structures of human MAP kinase kinase 1 (MEK1) and MEK2 describe novel noncompetitive kinase inhibition. *Nat. Struct. Mol. Biol.* **11**, 1192–1197 (2004). doi: 10.1038/nsmb859; pmid: 15543157
26. A. P. Bento *et al*., The ChEMBL bioactivity database: An update. *Nucleic Acids Res.* **42**, D1083–D1090 (2014). doi: 10.1093/nar/gkt1031; pmid: 24214965
27. A. Fauster *et al*., A cellular screen identifies ponatinib and pazopanib as inhibitors of necroptosis. *Cell Death Dis.* **6**, e1767 (2015). doi: 10.1038/cddis.2015.130; pmid: 25996294
28. K. Clark *et al*., Phosphorylation of CRTC3 by the salt-inducible kinases controls the interconversion of classically activated and regulatory macrophages. *Proc. Natl. Acad. Sci. U.S.A.* **109**, 16986–16991 (2012). doi: 10.1073/pnas.1215450109; pmid: 23033494
29. J. Ozanne, A. R. Prescott, K. Clark, The clinically approved drugs dasatinib and bosutinib induce anti-inflammatory macrophages by inhibiting the salt-inducible kinases. *Biochem. J.* **465**, 271–279 (2015). doi: 10.1042/BJ20141165; pmid: 25351958
30. T. S. Gujral, L. Peshkin, M. W. Kirschner, Exploiting polypharmacology for drug target deconvolution. *Proc. Natl. Acad. Sci. U.S.A.* **111**, 5048–5053 (2014). doi: 10.1073/pnas.1403080111; pmid: 24707051
31. A. C. Peterson, J. D. Russell, D. J. Bailey, M. S. Westphall, J. J. Coon, Parallel reaction monitoring for high resolution and high mass accuracy quantitative, targeted proteomics. *Mol. Cell. Proteomics* **11**, 1475–1488 (2012). doi: 10.1074/mcp.O112.020131; pmid: 22865924
32. S. Gallien *et al*., Targeted proteomic quantification on quadrupole-orbitrap mass spectrometer. *Mol. Cell. Proteomics* **11**, 1709–1723 (2012). doi: 10.1074/mcp.O112.019802; pmid: 22962056
33. E. Ardini *et al*., The TPM3-NTRK1 rearrangement is a recurring event in colorectal carcinoma and is associated with tumor sensitivity to TRKA kinase inhibition. *Mol. Oncol.* **8**, 1495–1507 (2014). doi: 10.1016/j.molonc.2014.06.001; pmid: 24962792
34. A. Vaishnavi *et al*., Oncogenic and drug-sensitive *NTRK1* rearrangements in lung cancer. *Nat. Med.* **19**, 1469–1472 (2013). doi: 10.1038/nm.3352; pmid: 24162815
35. P. J. Cook *et al*., Somatic chromosomal engineering identifies BCAN-NTRK1 as a potent glioma driver and therapeutic target. *Nat. Commun.* **8**, 15987 (2017). doi: 10.1038/ncomms15987; pmid: 28695888
36. L. Tang *et al*., Crystal structure of pyridoxal kinase in complex with roscovitine and derivatives. *J. Biol. Chem.* **280**, 31220–31229 (2005). doi: 10.1074/jbc.M500805200; pmid: 15985434
37. J. A. Winger, O. Hantschel, G. Superti-Furga, J. Kuriyan, The structure of the leukemia drug imatinib bound to human quinone reductase 2 (NQO2). *BMC Struct. Biol.* **9**, 7 (2009). doi: 10.1186/1472-6807-9-7; pmid: 19236722
38. S. Klaeger *et al*., Chemical proteomics reveals ferrochelatase as a common off-target of kinase inhibitors. *ACS Chem. Biol.* **11**, 1245–1254 (2016). doi: 10.1021/acschembio.5b01063; pmid: 26863403
39. M. M. Savitski *et al*., Tracking cancer drugs in living cells by thermal profiling of the proteome. *Science* **346**, 1255784 (2014). doi: 10.1126/science.1255784; pmid: 25278616
40. C. Borgo *et al*., Protein kinase CK2 potentiates translation efficiency by phosphorylating eIF3j at Ser127. *Biochim. Biophys. Acta* **1853**, 1693–1701 (2015). doi: 10.1016/j.bbamcr.2015.04.004; pmid: 25887626
41. H. Koch *et al*., Phosphoproteome profiling reveals molecular mechanisms of growth-factor-mediated kinase inhibitor resistance in EGFR-overexpressing cancer cells. *J. Proteome Res.* **15**, 4490–4504 (2016). doi: 10.1021/acs.jproteome.6b00621; pmid: 27794612
42. P. Mertins *et al*., Proteogenomics connects somatic mutations to signalling in breast cancer. *Nature* **534**, 55–62 (2016). doi: 10.1038/nature18003; pmid: 27251275
43. Y. Li *et al*., Network-based approach identified cell cycle genes as predictor of overall survival in lung adenocarcinoma patients. *Lung Cancer* **80**, 91–98 (2013). doi: 10.1016/j.lungcan.2012.12.022; pmid: 23357462
44. A. Lin, C. J. Giuliano, N. M. Sayles, J. M. Sheltzer, CRISPR/Cas9 mutagenesis invalidates a putative cancer dependency targeted in on-going clinical trials. *eLife* **6**, e24179 (2017). doi: 10.7554/eLife.24179; pmid: 28337968
45. H.-T. Huang *et al*., MELK is not necessary for the proliferation of basal-like breast cancer cells. *eLife* **6**, e26693 (2017). doi: 10.7554/eLife.26693; pmid: 28926338
46. S. Heinzlmeir *et al*., Chemical proteomics and structural biology define EPHA2 inhibition by clinical kinase drugs. *ACS Chem. Biol.* **11**, 3400–3411 (2016). doi: 10.1021/acschembio.6b00709; pmid: 27768280
47. E. Buchdunger *et al*., Abl protein-tyrosine kinase inhibitor STI571 inhibits in vitro signal transduction mediated by c-kit and platelet-derived growth factor receptors. *J. Pharmacol. Exp. Ther.* **295**, 139–145 (2000). pmid: 10991971
48. F. M. Yakes *et al*., Cabozantinib (XL184), a novel MET and VEGFR2 inhibitor, simultaneously suppresses metastasis, angiogenesis, and tumor growth. *Mol. Cancer Ther.* **10**, 2298–2308 (2011). doi: 10.1158/1535-7163.MCT-11-0264; pmid: 21926191
49. C. Choudhary *et al*., Mislocalized activation of oncogenic RTKs switches downstream signaling outcomes. *Mol. Cell* **36**, 326–339 (2009). doi: 10.1016/j.molcel.2009.09.019; pmid: 19854140
50. J.-W. Lu *et al*., Cabozantinib is selectively cytotoxic in acute myeloid leukemia cells with *FLT3*-internal tandem duplication (FLT3-ITD). *Cancer Lett.* **376**, 218–225 (2016). doi: 10.1016/j.canlet.2016.04.004; pmid: 27060207
51. H. Hahne *et al*., DMSO enhances electrospray response, boosting sensitivity of proteomic experiments. *Nat. Methods* **10**, 989–991 (2013). doi: 10.1038/nmeth.2610; pmid: 23975139
52. J. Cox, M. Mann, MaxQuant enables high peptide identification rates, individualized p.p.b.-range mass accuracies and proteome-wide protein quantification. *Nat. Biotechnol.* **26**, 1367–1372 (2008). doi: 10.1038/nbt.1511; pmid: 19029910

Downloaded from http://science.sciencemag.org/ on November 30, 2017

53. J. Cox *et al*., Andromeda: A peptide search engine integrated into the MaxQuant environment. *J. Proteome Res.* **10**, 1794–1805 (2011). doi: 10.1021/pr101065j; pmid: 21254760
54. J. Cox *et al*., Accurate proteome-wide label-free quantification by delayed normalization and maximal peptide ratio extraction, termed MaxLFQ. *Mol. Cell. Proteomics* **13**, 2513–2526 (2014). doi: 10.1074/mcp.M113.031591; pmid: 24942700
55. C. Ritz, F. Baty, J. C. Streibig, D. Gerhard, Dose-response analysis using R. *PLOS ONE* **10**, e0146021 (2015). doi: 10.1371/journal.pone.0146021; pmid: 26717316
56. S. Lemeer, C. Zörgiebel, B. Ruprecht, K. Kohl, B. Kuster, Comparing immobilized kinase inhibitors and covalent ATP probes for proteomic profiling of kinase expression and drug selectivity. *J. Proteome Res.* **12**, 1723–1731 (2013). doi: 10.1021/pr301073j; pmid: 23495751
57. H. Thorvaldsdóttir, J. T. Robinson, J. P. Mesirov, Integrative Genomics Viewer (IGV): High-performance genomics data visualization and exploration. *Brief. Bioinform.* **14**, 178–192 (2013). doi: 10.1093/bib/bbs017; pmid: 22517427
58. J. T. Robinson *et al*., Integrative genomics viewer. *Nat. Biotechnol.* **29**, 24–26 (2011). doi: 10.1038/nbt.1754; pmid: 21221095
59. B. Ruprecht *et al*., Comprehensive and reproducible phosphopeptide enrichment using iron immobilized metal ion affinity chromatography (Fe-IMAC) columns. *Mol. Cell. Proteomics* **14**, 205–215 (2015). doi: 10.1074/mcp.M114.043109; pmid: 25394399
60. J. Rappsilber, M. Mann, Y. Ishihama, Protocol for micro-purification, enrichment, pre-fractionation and storage of peptides for proteomics using StageTips. *Nat. Protoc.* **2**, 1896–1906 (2007). doi: 10.1038/nprot.2007.261; pmid: 17703201
61. B. MacLean *et al*., Skyline: An open source document editor for creating and analyzing targeted proteomics experiments. *Bioinformatics* **26**, 966–968 (2010). doi: 10.1093/bioinformatics/btq054; pmid: 20147306
62. A. M. Gholami *et al*., Global proteome analysis of the NCI-60 cell line panel. *Cell Rep.* **4**, 609–620 (2013). doi: 10.1016/j.celrep.2013.07.018; pmid: 23933261
63. W. Kabsch, Integration, scaling, space-group assignment and post-refinement. *Acta Crystallogr. D Biol. Crystallogr.* **66**, 133–144 (2010). doi: 10.1107/S0907444909047374; pmid: 20124693
64. W. Kabsch, XDS. *Acta Crystallogr. D Biol. Crystallogr.* **66**, 125–132 (2010). doi: 10.1107/S0907444909047337; pmid: 20124692
65. K. Diederichs, P. A. Karplus, Better models by discarding data?. *Acta Crystallogr. D Biol. Crystallogr.* **69**, 1215–1222 (2013). doi: 10.1107/S0907444913001121; pmid: 23793147
66. P. Evans, Resolving some old problems in protein crystallography. *Science* **336**, 986–987 (2012). doi: 10.1126/science.1222162; pmid: 22628641
67. P. A. Karplus, K. Diederichs, Linking crystallographic model and data quality. *Science* **336**, 1030–1033 (2012). doi: 10.1126/science.1218231; pmid: 22628654
68. M. D. Winn *et al*., Overview of the *CCP*4 suite and current developments. *Acta Crystallogr. D Biol. Crystallogr.* **67**, 235–242 (2011). doi: 10.1107/S0907444910045749; pmid: 21460441
69. G. N. Murshudov, A. A. Vagin, E. J. Dodson, Refinement of macromolecular structures by the maximum-likelihood method. *Acta Crystallogr. D Biol. Crystallogr.* **53**, 240–255 (1997). doi: 10.1107/S0907444996012255; pmid: 15299926
70. G. N. Murshudov *et al*., *REFMAC*5 for the refinement of macromolecular crystal structures. *Acta Crystallogr. D Biol. Crystallogr.* **67**, 355–367 (2011). doi: 10.1107/S0907444911001314; pmid: 21460454
71. P. Emsley, B. Lohkamp, W. G. Scott, K. Cowtan, Features and development of *Coot*. *Acta Crystallogr. D Biol. Crystallogr.* **66**, 486–501 (2010). doi: 10.1107/S0907444910007493; pmid: 20383002
72. E. Krissinel, K. Henrick, Secondary-structure matching (SSM), a new tool for fast protein structure alignment in three dimensions. *Acta Crystallogr. D Biol. Crystallogr.* **60**, 2256–2268 (2004). doi: 10.1107/S0907444904026460; pmid: 15572779
73. A. C. Wallace, R. A. Laskowski, J. M. Thornton, LIGPLOT: A program to generate schematic diagrams of protein-ligand interactions. *Protein Eng.* **8**, 127–134 (1995). doi: 10.1093/protein/8.2.127; pmid: 7630882
74. G. Canevari *et al*., Structural insight into maternal embryonic leucine zipper kinase (MELK) conformation and inhibition toward structure-based drug design. *Biochemistry* **52**, 6380–6387 (2013). doi: 10.1021/bi4005864; pmid: 23914841
75. T. G. G. Battye, L. Kontogiannis, O. Johnson, H. R. Powell, A. G. W. Leslie, *iMOSFLM*: A new graphical interface for diffraction-image processing with *MOSFLM*. *Acta Crystallogr. D Biol. Crystallogr.* **67**, 271–281 (2011). doi: 10.1107/S0907444910048675; pmid: 21460445
76. P. Evans, Scaling and assessment of data quality. *Acta Crystallogr. D Biol. Crystallogr.* **62**, 72–82 (2006). doi: 10.1107/S0907444905036693; pmid: 16369096
77. A. J. McCoy *et al*., *Phaser* crystallographic software. *J. Appl. Crystallogr.* **40**, 658–674 (2007). doi: 10.1107/S0021889807021206; pmid: 19461840
78. J. R. Wiśniewski, A. Zougman, N. Nagaraj, M. Mann, Universal sample preparation method for proteome analysis. *Nat. Methods* **6**, 359–362 (2009). doi: 10.1038/nmeth.1322; pmid: 19377485
79. S. Tyanova *et al*., The Perseus computational platform for comprehensive analysis of (prote)omics data. *Nat. Methods* **13**, 731–740 (2016). doi: 10.1038/nmeth.3901; pmid: 27348712
80. D. Szklarczyk *et al*., STRING v10: Protein–protein interaction networks, integrated over the tree of life. *Nucleic Acids Res.* **43**, D447–D452 (2015). doi: 10.1093/nar/gku1003; pmid: 25352553
81. Z. Wu, A. M. Gholami, B. Kuster, Systematic identification of the HSP90 candidate regulated proteome. *Mol. Cell. Proteomics* **11**, M111.016675 (2012). doi: 10.1074/mcp.M111.016675; pmid: 22337586
82. V. Ermolayev *et al*., Early recognition of lung cancer by integrin targeted imaging in K-ras mouse model. *Int. J. Cancer* **137**, 1107–1118 (2015). doi: 10.1002/ijc.29372; pmid: 25450481
83. G. Kayser *et al*., Simultaneous multi-antibody staining in non-small cell lung cancer strengthens diagnostic accuracy especially in small tissue samples. *PLOS ONE* **8**, e56333 (2013). doi: 10.1371/journal.pone.0056333; pmid: 23418554
84. H. Polzer, H. Janke, D. Schmid, W. Hiddemann, K. Spiekermann, Casitas B-lineage lymphoma mutants activate AKT to induce transformation in cooperation with class III receptor tyrosine kinases. *Exp. Hematol.* **41**, 271–280 (2013). doi: 10.1016/j.exphem.2012.10.016; pmid: 23127761
85. H. Janke *et al*., Activating FLT3 mutants show distinct gain-of-function phenotypes in vitro and a characteristic signaling pathway profile associated with prognosis in acute myeloid leukemia. *PLOS ONE* **9**, e89560 (2014). doi: 10.1371/journal.pone.0089560; pmid: 24608088
86. H. Polzer *et al*., Individualized treatment strategy with small-molecular inhibitors in acute myeloid leukemia with concurrent FLT3-ITD and FLT3-TKD mutation. *J. Clin. Case Rep.* **5**, 622 (2015). doi: 10.4172/2165-7920.1000622
87. B. A. Rabinovich *et al*., Visualizing fewer than 10 mouse T cells with an enhanced firefly luciferase in immunocompetent mouse models of cancer. *Proc. Natl. Acad. Sci. U.S.A.* **105**, 14342–14346 (2008). doi: 10.1073/pnas.0804105105; pmid: 18794521
88. N. Terziyska, C. Castro Alves, V. Groiss, K. Schneider, K. Farkasova, M. Ogris, E. Wagner, H. Ehrhardt, R. J. Brentjens, U. zur Stadt, M. Horstmann, L. Quintanilla-Martinez, I. Jeremias, In vivo imaging enables high resolution preclinical trials on patients' leukemia cells growing in mice. *PLOS ONE* **7**, e52798 (2012). doi: 10.1371/journal.pone.0052798; pmid: 23300782

ACKNOWLEDGMENTS

The data reported here are tabulated in the main paper and the supplementary materials. We want to thank J. Mergner, F. Seefried, D. Wang, A. Hubauer, M. Kroetz-Fahning, A. Klaus, S. Silingas, L.-H. Li, L. Wanat (all from TUM), B. Tizazu (LMU), and M. AbuJarour (SAP) for technical assistance. M. Fritschle is acknowledged for animal handling. E. Kunold and S. Sieber are acknowledged for measurement of phosphosamples. A.F. and A.W. thank U. Buchholz, C.-M. Pflüger, and A. Voss for technical assistance. D.P.Z. gratefully acknowledges funding from the Bundesministerium für Bildung und Forschung (BMBF) (grant 031L0008A—ProteomeTools). A.W. and A.F. gratefully acknowledge the financial support of the Deutsche Forschungsgemeinschaft (DFG) (SFB 824 TP Z02), BMBF (grant 01ZX1310B.01KT16015), and Deutsche Krebshilfe (grant 70112617). J.R. is grateful for European Research Council (ERC) Advanced Grant (FP7, grant agreement 322865). K.G., K.S., and H.P. are grateful for funding through DFG SFB1243. N.T. is funded by Institutional grant IUT60-20 and personal grant PUT736 from the Estonian Research Council. S.S. thanks Fonds der Chemischen Industrie. I.J. is thankful for ERC Consolidator Grant 681524, German Research Foundation, Collaborative Research Center 1243 "Genetic and epigenetic evolution of hematopoietic neoplasms," and the Mildred Scheel Professorship from German Cancer Aid. B.K. is an inventor on the patent EP20060763568 held by GlaxoSmithKline that covers the kinobeads technology. The proteomic data are available at the ProteomeXchange Consortium (http://proteomecentral.proteomexchange.org) via the PRIDE partner repository with the data set identifier PXD005336, as well as at ProteomicsDB (www.proteomicsdb.org) with the data set identifier PRDB004257. Compound selectivity data can also be explored at http://129.187.44.58:7575/. Crystal data are available at PDB protein database at www.rcsb.org/pdb with the following PDB accession codes: 5LBW, 5LBY, 5LBZ, 5M5A, 5MAF, 5MAG, 5MAH, and 5MAI. Supplementary materials are available as part of this Research Article, in the ProteomeXchange repository, and in the ProteomicsDB. Tables S1 and S2 contain direct links to the summary PDFs, containing the results of each drug profiling and the interactive visualizations in ProteomicsDB. H.H. is the cofounder, shareholder, and chief executive officer of OmicScouts, a company providing proteomic and chemical proteomic services. M.W. and B.K. are cofounders and shareholders of OmicScouts. They have no operational role in the company.

SUPPLEMENTARY MATERIALS

www.sciencemag.org/content/358/6367/eaan4368/suppl/DC1
Supplementary Text
Figs. S1 to S10
Tables S1 to S17
References (*89*–*123*)

13 April 2017; accepted 20 September 2017
10.1126/science.aan4368

Downloaded from http://science.sciencemag.org/ on November 30, 2017

Science

The target landscape of clinical kinase drugs

Susan Klaeger, Stephanie Heinzlmeir, Mathias Wilhelm, Harald Polzer, Binje Vick, Paul-Albert Koenig, Maria Reinecke, Benjamin Ruprecht, Svenja Petzoldt, Chen Meng, Jana Zecha, Katrin Reiter, Huichao Qiao, Dominic Helm, Heiner Koch, Melanie Schoof, Giulia Canevari, Elena Casale, Stefania Re Depaolini, Annette Feuchtinger, Zhixiang Wu, Tobias Schmidt, Lars Rueckert, Wilhelm Becker, Jan Huenges, Anne-Kathrin Garz, Bjoern-Oliver Gohlke, Daniel Paul Zolg, Gian Kayser, Tonu Vooder, Robert Preissner, Hannes Hahne, Neeme Tõnisson, Karl Kramer, Katharina Götze, Florian Bassermann, Judith Schlegl, Hans-Christian Ehrlich, Stephan Aiche, Axel Walch, Philipp A. Greif, Sabine Schneider, Eduard Rudolf Felder, Juergen Ruland, Guillaume Médard, Irmela Jeremias, Karsten Spiekermann and Bernhard Kuster

Science **358** (6367), eaan4368.
DOI: 10.1126/science.aan4368

An atlas for drug interactions

Kinase inhibitors are an important class of drugs that block certain enzymes involved in diseases such as cancer and inflammatory disorders. There are hundreds of kinases within the human body, so knowing the kinase "target" of each drug is essential for developing successful treatment strategies. Sometimes clinical trials can fail because drugs bind more than one target. Yet sometimes off-target effects can be beneficial, and drugs can be repurposed for treatment of additional diseases. Klaeger *et al.* performed a comprehensive analysis of 243 kinase inhibitors that are either approved for use or in clinical trials. They provide an open-access resource of target summaries that could help researchers develop better drugs, understand how existing drugs work, and design more effective clinical trials.

Science, this issue p. eaan4368

ARTICLE TOOLS http://science.sciencemag.org/content/358/6367/eaan4368

REFERENCES This article cites 122 articles, 33 of which you can access for free
http://science.sciencemag.org/content/358/6367/eaan4368#BIBL

PERMISSIONS http://www.sciencemag.org/help/reprints-and-permissions

Use of this article is subject to the Terms of Service

Science (print ISSN 0036-8075; online ISSN 1095-9203) is published by the American Association for the Advancement of Science, 1200 New York Avenue NW, Washington, DC 20005. 2017 © The Authors, some rights reserved; exclusive licensee American Association for the Advancement of Science. No claim to original U.S. Government Works. The title *Science* is a registered trademark of AAAS.

Downloaded from http://science.sciencemag.org/ on November 30, 2017